Physics – Uspekhi **65** (8) 789 – 811 (2022)

REVIEWS OF TOPICAL PROBLEMS PACS numbers: **07.60. – j, 42.62. – b, 42.70. – a, 42.79. – e, 42.82. – m,** 78.20.Fm

Phase singularities and optical vortices in photonics

A P Porfirev, A A Kuchmizhak, S O Gurbatov, S Juodkazis, S N Khonina, Yu N Kulchin

DOI: https://doi.org/10.3367/UFNe.2021.07.039028

Contents

Abstract. Since the second half of the 20th century, ideas to develop methods for the formation of optical vortices (OVs) or OV beams — regions of circular motion of energy flow in an electromagnetic wave around so-called phase singularity points — have become widespread. Such optical beams are unique because of the special spiral shape of the wave front, endowing them with orbital angular momentum (OAM) that can be transferred to matter and cause rotation of nano- and micro-objects. Presently, OV beams are actively used to solve both applied and fundamental problems in optics and photonics. We systematically discuss the development stages and the main advantages and disadvantages of methods for the formation of OV beams, from the appearance of phase singularities in light scattering in inhomogeneous media to the latest developments in vortex microlasers for controlled generation of light fields with a predefined OAM on nano- and microscales.

Keywords: singular optics, optical vortices, topological charge, spiral phase plate, spin-orbit interaction, fork-shaped holograms, metasurfaces, integrated optical elements, laser nanofabrication

A P Porfirev [1,2,*], **A A Kuchmizhak** [3,4,**], **S O Gurbatov** [3,5], **S Juodkazis** [6,7], **S N Khonina** [1,2], **Yu N Kulchin** [3,5]
[1] Image Processing Systems Institute–Branch of the Federal Scientific Research Centre Crystallography and Photonics of the Russian Academy of Sciences, ul. Molodogvardeiskaya 151, 443001 Samara, Russian Federation
[2] Samara National Research University, Moskovskoe shosse 34, 443086 Samara, Russian Federation
[3] Institute of Automation and Control Processes, Far Eastern Branch of the Russian Academy of Sciences, ul. Radio 5, 690041 Vladivostok, Russian Federation
[4] Far Eastern Federal University, Ajax 10, Russky island, 690922 Vladivostok, Russian Federation
[5] Pacific Quantum Center, Far Eastern Federal University, Ajax 10, Russky island, 690922 Vladivostok, Russian Federation
[6] Swinburne University of Technology, John St., Hawthorn 3122, Victoria, Australia
[7] Melbourne Centre for Nanofabrication, ANFF, 151 Wellington Road, Clayton, VIC 3168, Australia
E-mail: [*] porfirev.alexey@gmail.com, [**] alex.iacp.dvo@mail.ru

Received 17 May 2021, revised 19 July 2021
Uspekhi Fizicheskikh Nauk **192** (8) 841 – 866 (2022)
Translated by S Alekseev

1. Introduction

Vortices are a common phenomenon in both animate and inanimate nature: they appear on the microscale, for example, as supercurrent eddies in superconducting materials, and on the macroscale as the motion of twisting gas in galaxies (for example, Jupiter's Great Red Spot is a giant vortex about 25,000 km in diameter). The formation of vortices can be observed in various technological devices and mechanisms, as well as in ocean currents and air flows. We note that vortices can have positive effects, for example, creating lift thrust for aircraft, but can also cause catastrophic destruction, generating tornadoes and hurricanes.

Since the second half of the 20th century, optical vortices (OVs) have begun to be widely studied; they are areas of circular motion of energy flow in an electromagnetic wave around so-called phase singularity points due to violations of the topological structure of the wave front. The growing interest in vortices in the optical range is primarily due to helical (spiral) dislocations of the wavefront that arise in

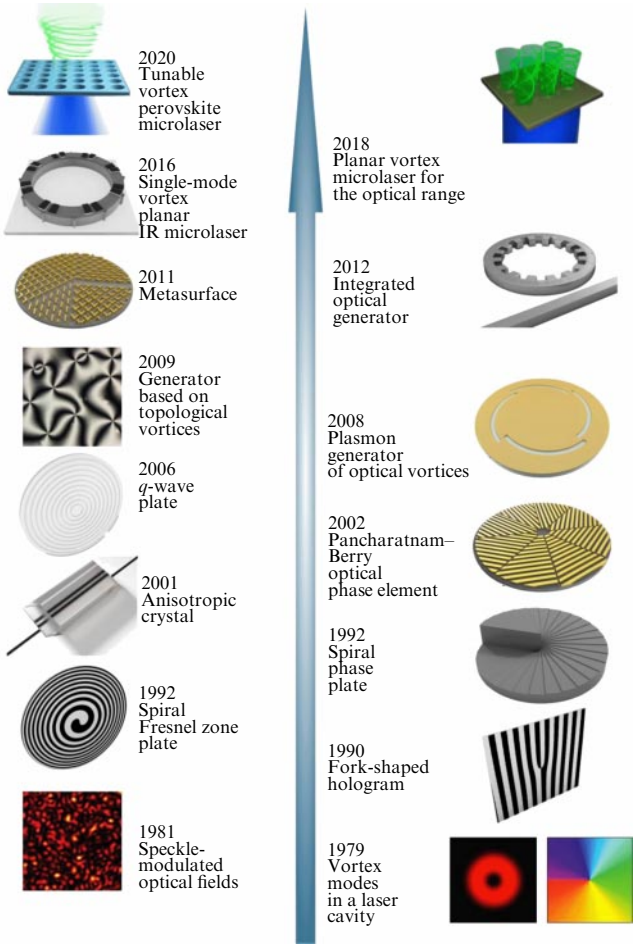

Figure 1. (Color online.) Schematic representation of the emergence and temporal evolution of OV generation methods, ranging from the random occurrence of phase singularities in speckle fields generated by the passage of laser beams through inhomogeneous media to recent results in the field of vortex microlasers used as active controlled OAM radiation generators on nano- and microscales.

them: the azimuthal change in the phase of the light field in the vicinity of such a dislocation is $2\pi\ell$ relative to the propagation axis, where ℓ is the number of turns on the wavefront per unit wavelength, also called the topological charge (TC) of the formed beam [1]. As was shown in 1992, such a phase distribution leads to the presence of an orbital angular momentum (OAM) equal to $\ell\hbar$ per photon (where $\hbar$ is Planck's constant) of the resultant vortex electromagnetic field [2]. The term 'optical vortex' itself was first introduced in 1989 [3] to emphasize the analogy between optical beams with a helical wave front and superfluid vortices.

Active studies of the formation of OV beams and their properties have led to the emergence of a new discipline called 'singular optics,' which studies the properties of OV beams and their formation mechanisms [4–6]. OV beams are widely used in many areas of modern photonics, including laser manipulation of microobjects, optical communications, superresolution confocal optical microscopy, laser processing of materials, and imaging optics [7, 8]. To date, various methods for the formation of OV beams have been developed based on both elements of classical optics (for example, combinations of cylindrical lenses) and diffractive optical elements, which allow forming not only single OV beams but also their one-, two-, and three-dimensional combinations, as well as metasurfaces, which have become widespread in the last decade because they allow OV beams to be formed by a fundamental transformation of the spin angular momentum (SAM) of light associated with circular polarization into its OAM.

An analysis of recent publications and trends shows that interest in OV beams, their properties, and their formation methods continues to grow [9–14]. More and more new areas of science and technology are involved in the field of possible applications of OAM light beams. An increasing number of experts are interested in studying the properties of such beams and in efficient and optimal methods for their formation for a specific range of problems. In this review, we systematically consider the stages in the development of methods for the formation of OV beams, starting from the random occurrence of phase singularities in speckle fields formed during the passage of laser beams through inhomogeneous media, and ending with recent results in the development of vortex microlasers, which are active and controllable generators of OAM-carrying radiation on the nano- and microscale (Fig. 1). We comparatively analyze the currently developed approaches to the formation of OV beams, their advantages and disadvantages, and the technological options for their implementation. In Section 10, we discuss one of the actively developing areas, largely ignored in the existing reviews, which is aimed at studying the interaction of intense OV beams with nanosize structures and materials for nanophotonics and precision laser fabrication of functional nanostructures.

2. Speckle fields: phase singularities in randomly inhomogeneous media

As is known, speckle fields are random interference patterns that arise when coherent laser radiation passes through a randomly inhomogeneous (turbulent) medium consisting of many regions with refractive index inhomogeneities (Fig. 2a) [15]. Such inhomogeneities cause amplitude and phase distortions, leading to the formation of a random intensity pattern due to the interference of scattered or refracted radiation. In 1974, Nye and Berry [1, 16] showed theoretically that a light wave propagating in air and reflected (scattered) on a rough surface contains phase singularity points, where the phase of a complex scalar wave

$$\psi(\mathbf{r},t)=\rho(\mathbf{r},t)\exp\left[\mathrm{i}\varphi(\mathbf{r},t)\right],\ \mathbf{r}=(x,y,z)\,, \tag{1}$$

is undefined. Such phase singularities appear at points where the real and imaginary parts of the complex amplitude of a scalar optical field vanish [5] and are typically associated with first-order OVs, those with the TC of the beam equal to 1. But in the general case of OVs arising in speckle fields, as has been shown in a number of studies [16–19], the phase changes nonlinearly when going around a phase singularity point in the azimuthal direction.

The first experimental demonstration of the appearance of phase singularities in a random speckle field was presented by Zel'dovich's group [20–22] in 1981. Further experimental studies were aimed at investigating the local properties and structure of the core of the OVs formed in this case [23], as well as their statistical properties, confirming the original theoretical predictions that had been made by Nye and Berry [1, 16]. Research in this area eventually led to the emergence of a new field called stochastic singular optics [24–27], which

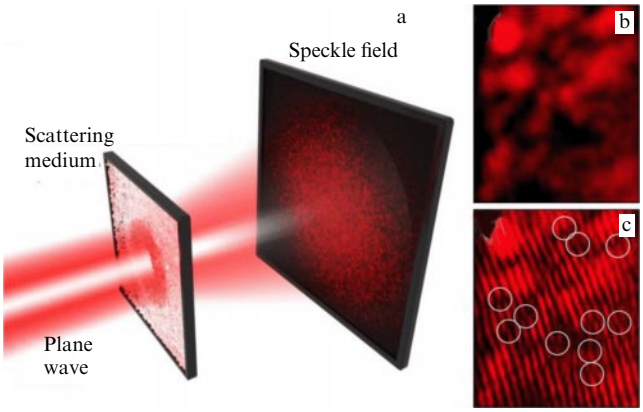

Figure 2. (Color online.) (a) Formation of a speckle field due to the interference of scattered waves during the passage of coherent laser radiation through a turbulent scattering medium. (b) Characteristic distribution of the intensity of the formed speckle field and (c) the result of its interference with an oblique plane wave, demonstrating the appearance of fork-shaped interference fringes (shown with white circles) characteristic of phase singularity points.

studies the general properties of phase singularities in random media.

In Fig. 2b, we show an enlarged cross section of a typical speckle field, where individual speckle structures and zero-intensity spots can be clearly distinguished. The phase singularities can be detected using the interference of the formed speckle field with a tilted plane wave, which is a standard method not only for demonstrating the occurrence of an OV but also for measuring its TC. In this case, the splitting of individual interference fringes into two, leading to the formation of fork-shaped fringes (Fig. 2c), indicates the appearance of a phase singularity point associated with a first-order OV. The splitting of the interference fringes into a larger number of fork-shaped fringes indicates the appearance of higher-order OVs. The absence of a higher-order OV in the example under discussion can be explained by the fact that such OVs are extremely unstable, even against small perturbations of the wavefront field, causing a decomposition of an ℓth-order OV into ℓ first-order OVs [28]. According to the topological charge conservation law, which states that the total TC arising on a closed surface is equal to zero [27, 29], the probability of the appearance of positively and negatively charged first-order OVs (those with a positive or negative TC) is the same. Thus, the total charge of all OVs appearing in the speckle field is equal to zero [30–32]. In the case of a typical speckle field with the average size of an individual speckle estimated as $\approx \lambda R/D$ (where D is the laser beam diameter, R is the distance between the image plane and the scattering medium, and λ is the radiation wavelength) [33], the average density of phase singularities and the associated OVs is approximately $(\Delta\theta)^2/\lambda^2$, where $\Delta\theta$ is the angular divergence of the beam [28, 30].

The extremely high sensitivity of speckle fields to any perturbations in the medium (vibrations, stresses, temperature changes, etc.) is well known; it leads to random distortions and a rearrangement of the structure of individual speckles and a related change in the structure of the formed OVs. Such spatiotemporal changes in the OV in dynamical speckle fields were studied in detail in [34–38], where a strong correlation was found between the displacement of the scattering medium used to create speckle structures and the corresponding displacement of the position of the formed OVs [34]. It is noteworthy that the OV trajectories turned out to be relatively short and winding for rapidly changing speckle structures and rather extended and more direct for slowly changing ones [35–37].

Thus, it can be concluded that speckle fields that can be formed using only a roughly polished glass slide represent the simplest way to generate OVs. In this case, however, it is impossible to control either the spatial position of individual OVs or the magnitude or sign of their TC associated with the structure of their phase distribution.

3. Formation of optical vortices at the laser cavity output

Phase singularities similar to those occurring in a random speckle field can also be created in a controlled way: for example, they can be directly generated at the output of a laser cavity. In 1979, Vaughan and Willets [39] used a high-power krypton-ion gas laser to observe the generation of an annular laser beam with a helical wavefront characteristic of OV beams [39]. They explained this effect by an increase in the contribution of higher-order intracavity modes when the laser was operated in the high-power regime. A combination of two orthogonal TEM_{01} modes forms the so-called hybrid TEM_{01}^{*} mode (Fig. 3) with an axially symmetric transverse intensity distribution and a helical wavefront. Frequency analysis and the study of two-beam interference of such hybrid laser modes showed the possibility of generating a laser beam with a helical in-phase surface [40]. Subsequently, the formation of a stable intensity distribution in the form of an annulus with a helical wave front was also observed in frequency-locked helium-neon lasers in the presence of an intracavity absorbing material [41]. This effect was explained by the interaction of the almost degenerate intracavity TEM_{01} and TEM_{10} modes of the helium–neon laser.

In 1989, Coullet and collaborators, by numerically solving the Maxwell–Bloch equations, demonstrated the appearance of a phase singularity of the electric field in a laser cavity with a large Fresnel number [3] and theoretically described a new state of the laser associated with the existence of a vortex solution of the electrodynamic laser equations

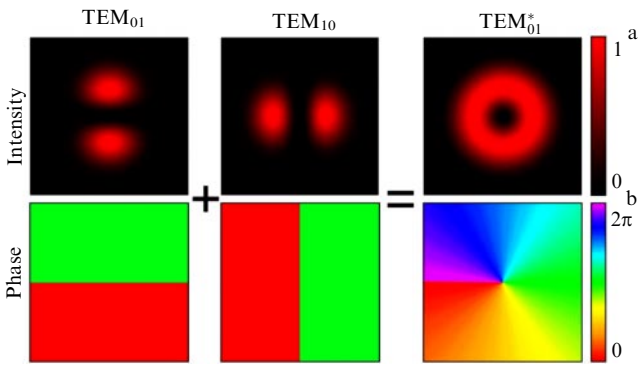

Figure 3. (Color online.) Combination of TEM_{01} and TEM_{10} modes to form a hybrid TEM_{01}^{*} mode with a helical wavefront. The TEM_{01} mode has a $\pi/2$ phase delay. (a) Intensity distributions. (b) Mode phase distributions. The total amplitude of the sum of the TEM_{01} and TEM_{10} modes is $i2^{-1/2}E_{01} + 2^{-1/2}E_{10} = (E_0 r/w)\exp(-r^2/w^2)\exp(i\varphi)$, where $E_{01} = 2^{1/2}E_0(r/w)\exp(-r^2/w^2)\sin\varphi$ and $E_{10} = 2^{1/2}E_0(r/w)\exp(-r^2/w^2)\cos\varphi$.

underlying mode locking. Later, by adjusting the position of the absorbing material inside the laser cavity to tune the required axial mode, the possibility of intracavity generation of first-, second-, and third-order OVs with high mode purity was demonstrated in an argon ion laser with a low Fresnel number [42].

In 1990, to demonstrate the bistability of the hybrid TEM_{01}^{*} laser mode associated with the presence of two stable vortex modes with opposite TC signs, Tamm and Weiss used an optically induced switching scheme based on reinjection of the laser output field into a laser cavity, but with a changed field phase [43]. The transverse mode converter used in this case, made of two cylindrical lenses and based on the astigmatic transformation of higher-order transverse modes, allowed distinguishing between two stable configurations of the spatial field. Later, Abramochkin and Volostnikov showed in [44] the possibility of using astigmatic optical systems containing two spherical and one cylindrical lens to convert nonvortex Hermite–Gauss laser beams into Laguerre–Gauss (LG) vortex beams.

We note that a similar optical system was also used in the very first demonstration that an LG vortex laser beam $LG_{\ell p}$ with TC ℓ and radial index p has an OAM equal to $\ell\hbar$ per photon [2]. It was the pivotal paper [2] that contributed to the further development of various methods for the direct generation of OV beams using lasers: a range of methods have developed, such as the coherent addition of two orthogonally polarized transverse modes inside a laser cavity [45], defocusing of radiation from a fiber laser diode in compact solid-state end pumping [46, 47], the use of a dielectric multilayer intracavity mirror with a resonant corrugated grating [48], optical pumping by a pulsed laser beam diffracted by a circular aperture [49, 50], various methods of off-axis pumping [51–54], the use of a segmented half-wave plate in the cavity of a titanium–sapphire laser [55], the use of a capillary fiber to adjust the shape of the laser pump beam [56, 57], birefringence-induced bifocusing in the laser cavity [58], the use of the Brewster effect in an optical element made of a convex and concave conical prism inside the laser cavity [59], annular beam pumping [60–66], mode selection with [67] or without [68] an intracavity element, the use of mirrors with defects to suppress oscillations of the lowest transverse intracavity modes [69–71], the use of an asymmetric cavity configuration [72–74] or a cavity with an antiresonant ring [75], the use of an optical parametric oscillator based on an optical cavity that rotates the image by 90° for each pass [76], the use of dynamical acoustic vortex gratings based on stimulated Mandelshtam–Brillouin scattering [77], and many more methods [10, 78–81].

The main advantage of the methods for direct generation of OV beams is the possibility of obtaining OV beams with a high average power up to 25 W [56, 82] and peak power up to 59 kW [83] in an extremely wide spectral range, from deep ultraviolet to infrared (IR) [57, 84–87]. At the same time, solutions were proposed to implement tunable generation of first-order OV beams in various IR ranges: 0.97–1.174 μm [88], 1.48–1.64 μm [89], 0.546–1.562 μm [90], 1.36–1.63 μm, 3.07–4.81 μm [91], and even 6–18 μm, i.e., covering the entire mid-IR range, which is interesting from the standpoint of applications of superresolution molecular spectroscopy [92]. In addition, intracavity generation methods make it possible to form higher-order OVs at the laser output with a TC greater than 200, an ideal beam quality, and a mode purity up to 100% [42, 50, 69, 85, 93–96]. With the use of Q-switched fiber vortex lasers, it is possible to tune the duration of the generated OV pulses; in this way, the possibility of generating pulses with a switchable duration of 1.098 ps and 542 fs was shown [97]. We also note that only methods of direct laser generation can ensure an extremely high repetition rate of the generated OV pulses, up to several ten or hundred MHz [98]. And the use of mode-locked fiber vortex lasers can provide additional tuning of the repetition rate of vector OV pulses with a mode purity above 97% in the frequency range of 15.65–626 MHz with a step of 15.65 MHz and with high stability [99].

4. Holographic methods for the formation of optical vortices

4.1 Fork-shaped holograms

In 1990, Soskin et al. proposed in [100] using the principles of holography for the out-of-cavity formation of OV beams. The holograms were binary fork-shaped amplitude structures, also called diffraction gratings with groove bifurcation in the center (Fig. 4). Such holograms can be used to simultaneously form OV beams with opposite TCs in conjugate diffraction orders [100]. In [100], the formation of higher-order optical beams was first demonstrated using computer-calculated holograms, which paved the way for the development of methods for the controlled formation of optical beams with predetermined parameters. In 1992, Heckenberg and colleagues presented a theoretical description of the diffraction of a Gaussian beam on a fork-shaped amplitude hologram and calculated the resultant field distributions [101]. The properties of OV beams (including those with a fractional TC) formed by such holograms were studied theoretically and experimentally somewhat later in [102–106].

A theoretical description of Fresnel and Fraunhofer diffraction of a Gaussian beam on fork-shaped gratings defined by a generalized transmission function that combines the cases of multilevel amplitude and binary gratings and their phase analogs was given in [107]. In a cylindrical coordinate system, the generalized transmission function is

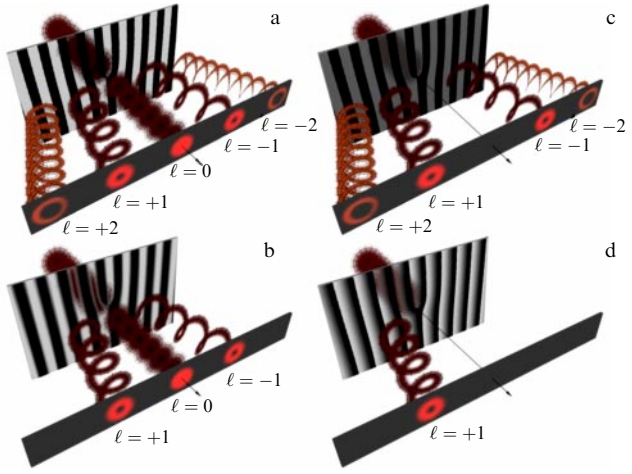

Figure 4. (Color online.) Formation of OV beams using various types of fork-shaped holograms: (a) binary amplitude grating, (b) sinusoidal amplitude grating, (c) binary phase grating, (d) glare phase grating.

defined as

$$T(r,\varphi) = \sum_{m=-\infty}^{\infty} t_m \exp\left[-\mathrm{i}m\left(\frac{2\pi}{D} r\cos\varphi - p\varphi\right)\right]$$
$$= t_0 + \sum_{m=1}^{\infty} t_m \exp\left[-\mathrm{i}m\left(\frac{2\pi}{D} r\cos\varphi - p\varphi\right)\right]$$
$$+ \sum_{m=1}^{\infty} t_{-m} \exp\left[\mathrm{i}m\left(\frac{2\pi}{D} r\cos\varphi - p\varphi\right)\right], \qquad (2)$$

where r and φ are polar coordinates in the plane of the grating, p is an integer one less than the number of strips into which the central strip of the grating is divided, D is the period of the rectilinear part of the grating, and t_m are transmittances, which are complex in the general case.

Depending on the method of realization of a hologram, four main types of fork-shaped gratings can be distinguished (see Fig. 4): binary amplitude, sinusoidal amplitude, binary phase, and glare phase beam gratings. For binary amplitude fork-shaped gratings, the coefficients t_m are $t_0 = 1/2$, $t_{\pm m=\pm(2m'-1)} = \mp \mathrm{i}/\pi(2m'-1)$, and $t_{\pm m=\pm 2m'} = 0$ $(m' = 1, 2, 3, \ldots)$. Such elements form a nonvortex beam in the zeroth diffraction order and OV beams with the TCs $\ell = \pm(2m'-1)p$ in odd diffraction orders, defined as $\pm(2m'-1)$ (Fig. 4a). It is noteworthy that the intensity of the beam in each subsequent diffraction order decreases as $1/\pi^2(2m'-1)^2$. In the case of an amplitude fork-shaped grating with a sinusoidal variation in optical density, only terms with $m = -1$, 0, and 1 remain in Eqn (2) (and, in addition, $t_1 = t_{-1} = t/2$), which means that only three beams are formed behind the grating: a nonvortex beam in the zeroth diffraction order and two OV beams with opposite TCs $\pm p$ in diffraction orders ± 1 (Fig. 4b). Although such an element allows completely suppressing the formation of higher-order beams, the beam formed in the zeroth order has a higher intensity than that in the case of a binary amplitude grating. The presence of such a phase-unmodulated beam in the zeroth diffraction order and of beams in higher diffraction orders, in combination with losses due to absorption, leads to a rather low efficiency in the formation of the required OV beams in the case of both amplitude-type elements. For example, the formation efficiency of a single OV beam in the first diffraction order is about 6% for a sinusoidal [108] and about 10% for a binary [109] fork-shaped amplitude hologram.

For the binary phase version of a fork-shaped grating with ideal transmission, the coefficients in Eqn (2) are $t_0 = \exp(\mathrm{i}k\alpha)\cos(k\beta)$, $t_{\pm m=\pm(2m'-1)} = \pm\exp(\mathrm{i}k\alpha)(2/\pi)[1/(2m'-1)]\times \sin(k\beta)$, and $t_{\pm 2m'} = 0$ $(m' = 1, 2, 3, \ldots)$, where $k\alpha$ is the phase offset delay and $k\beta$ is the phase modulation amplitude. For example, for $k\beta = \pi/2$, we have $t_0 = 0$, $t_{\pm m=\pm(2m'-1)} = \pm\exp(\mathrm{i}k\alpha)(2/\pi)[1/(2m'-1)]$, $t'_{\pm 2m} = 0$, and the corresponding phase element forms two OV beams with opposite TCs $\ell = \pm(2m'-1)p$ in the $\pm(2m'-1)$th diffractive orders without any unmodulated beam in the zeroth order (Fig. 3c). An analysis of the transmission coefficients of the phase hologram shows that the deviation of $k\beta$ from $\pi/2$ results in the appearance of a nonvortex beam in the zeroth diffraction order, while the TCs of the OV beams formed in ± 1st diffraction orders do not change [110]. We note that the zeroth order also appears when the ratio between the width of the phase strips over the grating period changes (which can be achieved by binarizing the phase function on a level above or below π). In this case, even diffraction orders $(\pm 2m')$ [111] are also formed, which are absent in the standard 'uniform' binarization method.

Finally, in the case of a glare phase fork-shaped grating, only the coefficient t_1 remains nonzero. In fact, the transmission function of the element in this case is given by the azimuthally variable term $\exp(\mathrm{i}\ell\varphi)$ times the traditional glare phase grating that directs a single formed OV beam of the ℓth order to the diffraction order $+1$ (Fig. 3d). Ideal versions of phase fork-shaped gratings allow suppressing the beam formed in the zeroth diffraction order, which results in a significant increase in the efficiency of the formation of the OV beam with the required TC, up to 40% for a binary grating [109] and more than 50% for a glare phase grating [112].

Theoretically, a nearly 100% conversion efficiency of the initial radiation into an OV beam (without reflection losses) can be achieved by using volume holograms with a built-in phase singularity [113–115]. For example, in [113], bichromated gelatin plates with an antireflection coating were shown to have a conversion efficiency exceeding 90% at a wavelength of 800 nm. The use of photorefractive glass allows an efficiency of almost 85% to be achieved at a wavelength of 1064 nm [116]. In addition, the damage threshold of such fork-shaped volume holograms can be quite high, more than 270 GW cm^{-2} [113, 117]. The combination of these properties, in principle, allows using fork-shaped holograms for the formation of OV beams with extremely high TCs, exceeding 10,000 in higher diffraction orders, although currently only OVs with the TC not exceeding 100 have been reported [118].

We note several important features of fork-shaped holograms for the formation of OV beams. First, when illuminated with an OV beam with a TC ℓ, such holograms form an OV with TCs $\ell + pn$ in higher diffraction orders (where n is the corresponding diffraction order number), together with an additional OV beam with the TC ℓ in the zeroth diffraction order [112, 119–122]. Second, the misalignment of the center of the incident beam and the bifurcation point of the hologram as well as a tilt of the incident beam relative to the normal to the surface of the hologram lead to a corresponding displacement of the vortex core and distortion of the annular shape of the generated OV beam intensity distribution [123–125]. A rigorous theoretical analysis of the incidence of the illuminating beam at large angles showed a transverse deformation of the formed OV beam (its compression in the transverse plane) [126, 127]. We also mention paper [128], which shows the evolution of the structure of first-order OV beams formed by a binary fork-shaped phase grating etched at the end of an optical fiber in the near-field zone. The use of such fibers allows implementing a fiber optical communication system that performs both multiplexing and demultiplexing of OV beams in schemes with mode multiplexing of channels by OAM [129].

To date, various popular methods have been used to produce and implement fork-shaped holograms: electron beam lithography [130, 131], the use of liquid crystal (LC) cells [132], direct laser micromachining of metal mirrors [133], photolithography [134], and many others. In fact, such elements can even be produced by simply printing computer-designed templates using digital laser printers and plotters and then converting these templates into transparent or reflective elements [135, 136]. For example, there are studies demonstrating the printing of fork-shaped holograms on transparent sheets using laser printers with a 600 dpi resolution [137]. It is noteworthy that the use of LC spatial light modulators (LCSLMs) makes it possible to implement fork-

shaped holograms with a dynamically tunable TC [138]. Such dynamically switched devices have been implemented, in particular, using inexpensive SLMs fabricated from materials extracted from used LC displays [139], employing polymer-dispersed LCs [140, 141] and a microlithographic utility installation based on a digital micromirror device [142, 143]. However, the characteristic tuning frequency for all LC devices does not exceed several ten hertz. Faster switching can be realized with blue-phase cholesteric LC devices [144], providing a switching time of about 500 μs.

4.2 Spiral Fresnel zone plates

In 1992, Heckenberg and collaborators proposed a new type of computer-calculated hologram for the formation of OV beams, the so-called spiral Fresnel zone plate (SFZP) [145]. The transmission function of an SFZP with a TC ℓ can be represented in polar coordinates (r, φ) as (Fig. 5a)

$$T(r, \varphi) = \exp\left\{\mathrm{i} \arg\left[\cos\left(\alpha r^2 + \ell\varphi\right)\right]\right\}, \qquad (3)$$

where $\alpha = \pi/\lambda f$ is a scaling parameter and f is the focal length on which the first-order SFZP is focused in the case of radiation with wavelength λ.

In contrast to fork-shaped holograms, SFZPs form OVs on the optical axis (Fig. 5a); all diffraction orders formed by such elements are located along the light beam propagation axis at different focal lengths [146]. At the same time, SFZPs are not without the drawbacks inherent in axial Gabor holograms [108, 147, 148]. For example, such optical elements do not allow separating the reconstructed beams from each other or from the incident light, and the binary structure of the elements gives rise to multiple images. In addition, it has been found that the quality of the OV beams formed by an SFZP decreases as the focal length modulus increases at a fixed waist radius of the illuminating beam [149]. Nevertheless, the unique properties of SFZPs allow them to be used in various applications, such as detection of wavefront helicity [150, 151], optical profilometry [152], the formation of vortex beams in the extreme ultraviolet range [153], optical microscopy [154], and the formation of the inverse energy flux [155]. Such elements can be used, among other things, to create stable 'rainbow' OV beams in white light that persist at sufficiently large distances (up to 80 m for a beam diameter of several millimeters), which is important for solving various fundamental and applied scientific problems [146].

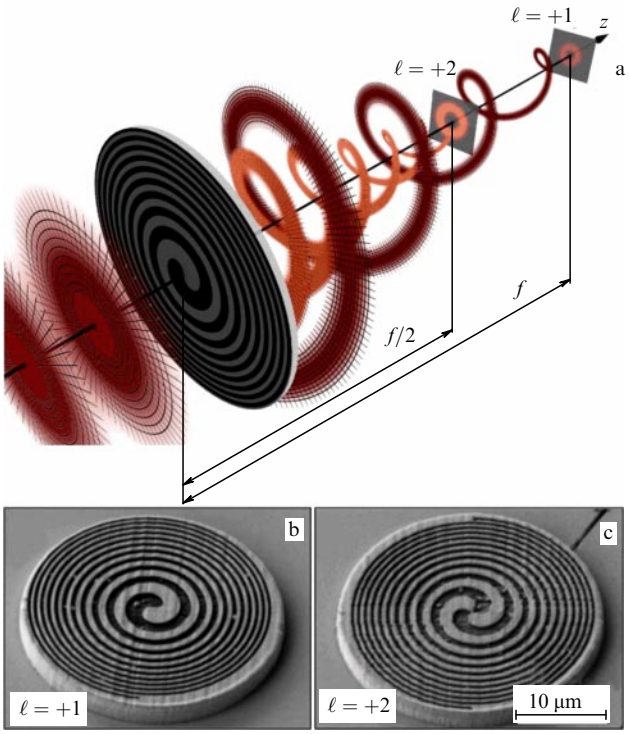

Figure 5. (Color online.) Formation of OV beams with SFZPs. (a) Schematic representation of the formation of a first-order OV beam ($\ell = +1$) using an SFZP. It can be clearly seen that, in contrast to diffraction orders inherent in fork-shaped holograms, diffraction orders formed by an SFZP and carrying OV beams with higher topological charges ($\ell \geqslant 1$) are located along the optical axis at different distances from the plane of the element. (b, c) Images of microsize SFZPs with $\ell = +1$ and $+2$ made using direct laser recording and subsequent ion beam processing. (Images from [162].)

Several new types of optical elements based on SFZPs have been developed for the formation of OV beams: a spiral zone plate (SZP) with an increased focus depth for the formation of OV beams extended along the propagation axis [156], a composite SZP for the formation of two OV beams at different distances along the propagation axis [157], a square binary SZP for the formation of OV beams with fourth-order rotational symmetry [158, 159], a Dammann SZP that forms a set of OV beams with opposite TCs (so-called dipole vortices) along the optical axes in the immediate vicinity of the focal region with a total efficiency of 70% for the first five diffraction orders [160], fractional SZPs forming OV beams with a fractional TC [161], a hybrid three-dimensional microelement combining an SFZP and a microaxicon [162, 163], an SFZP with a displaced center for the formation of superpositions of OV beams [164], a zone plate with a helically shifted phase for the formation of various types of OV beams with a controlled TC [165], various types of fractal SFZPs with an increased focusing depth of the OV beams formed on the propagation axis of the OV beams and with the diffraction efficiency of the OV beam in the first diffraction order increased to 8.5% [166–169], and even a single-focus SFZP, an element that combines the structure of an SFZP and a Gabor zone plate to form a single OV beam with an efficiency of about 10% [170].

To fabricate SFZPs, approaches similar to those used to fabricate fork-shaped holograms and gratings can be used: lithography and liquid etching methods [160, 170], LCSLMs [149], projection lithography [171], direct laser recording methods [162, 163, 172, 173] (Fig. 5b, c), laser printing [174], electron beam lithography [152, 154, 158], and element template transfer using an electronic exposure device [165]. An interesting option for fabricating SFZPs on the surface of a zinc oxide crystal by etching was shown in [175]: such a diffractive element allows not only forming an optical beam but also performing a nonlinear frequency conversion of the initial radiation to higher-order harmonics. The main advantages of SFZPs are their simple binary structure and the possibility of forming OV beams located on the optical axis. However, the SFZP conversion efficiency is quite low, even compared to the conversion efficiency of binary fork-shaped phase holograms.

4.3 Other types of computer-calculated holograms

Modern computer technology allows greatly simplifying and significantly accelerating the calculation of holograms, providing an efficient method for fabricating nonconventional elements for the formation of OV beams. In the

general case, by combining the azimuthal phase factor $\exp(i\ell\varphi)$ with the transmission function of some other functional optical element, a new type of OV beam generator with extended functionality can be created. In this section, we briefly describe these more complex types of holograms and their main characteristics.

For example, the use of a composite element — a spiral fork-shaped plate that combines the SFZP and the fork-shaped binary phase grating — allows forming two off-axis OV beams with the TC determined by the sum and difference of the TCs of the corresponding SFZP and the fork-shaped grating [176]. A helical axicon with the axicon transmission function modified by a helical phase factor has been demonstrated in several papers [162, 177–179] for the formation of higher-order quasi-Bessel OV beams. A similar strategy was applied to create a vortex lens with the required focal length and a TC of the formed OV beam up to 200, attained by multiplying the element transmission function with azimuthal phase modulation by the Fresnel lens transmission function [180–183]. Also noteworthy is the spiral fractal zone plate, which is a combination of the fractal zone plate and the spiral phase [184], and the vortex 'devil's' lens [185–187], which is a phase 'devil's' lens (described by Cantor's 'devil's staircase' function) modulated by a helical phase structure with a theoretical conversion efficiency reaching 60% [188].

In addition, calculated computer holograms allow forming certain types of structured OV laser beams such as higher-order LG modes [189–192], Bessel beams [193, 194], Mathieu beams [195], Hankel beams [196, 197], and new types of OV beams, including multi-annulus OV beams [198], elliptical OV beams [199, 200], hypergeometric laser beams [201–204], 'ideal' optical vortices (IOVs) with various profiles [205–209], nondiffracting Bessel beams with complex displacement [210], asymmetric LG beams [211], elliptical OV beams [212], and many others [213–217].

In most cases, dynamical SLMs are the most convenient commercially available tool for the implementation of complex computer-calculated holograms, and SLM-based holograms have therefore become widespread in the field of formation of controlled and dynamically tunable OV beams. However, SLMs have a slow response time, as noted above, and are rather bulky. In addition, due to the rather low damage threshold of the active matrix of displays, they must be used with extreme care in combination with high-intensity pulsed laser radiation. Therefore, such devices, despite all their unique properties, also have significant drawbacks, and hence the problem of finding new flexible approaches to the formation of OV beams remains relevant.

5. Spiral phase plates

A spiral phase plate (SPP) with a TC ℓ is an optical element with the azimuthally varying thickness $h = \ell\lambda\varphi/2\pi\Delta n$, where Δn is the difference between the refractive indices of the SPP material and the ambient medium. An SPP works by directly applying the helical phase shift $\exp(i\ell\varphi)$ to the incident laser beam (Fig. 6a), allowing almost 100% of the incident radiation energy to be converted into the OV beam. The complex transmission function of an SPP with radius R in polar coordinates is given by

$$T(r,\varphi) = \mathrm{circ}\left(\frac{r}{R}\right)\exp(i\ell\varphi). \qquad (4)$$

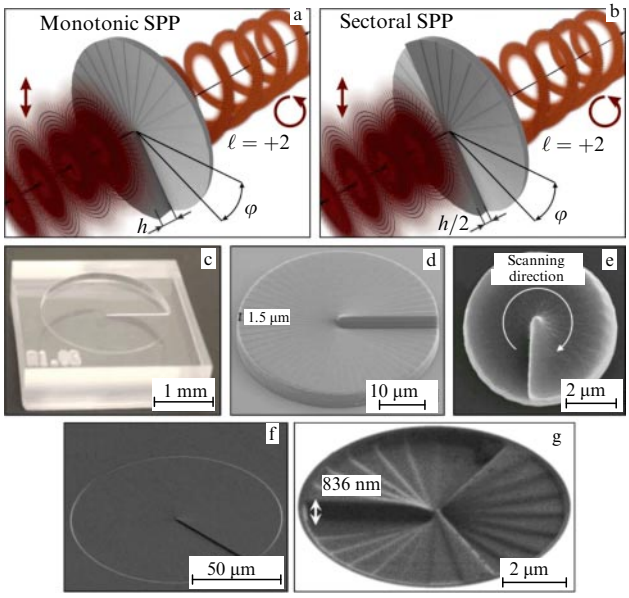

Figure 6. (Color online.) Schematic representation of the formation of an OV beam using an SPP with a (a) monotonic and (b) sectoral phase increase from 0 to 2π. Both elements shown allow the formation of an OV beam with $\ell = 3$. SPP images made using: (c) milling, (d, e) direct laser recording, (f) electron beam lithography, and (g) ion beam lithography. (Images c–g are respectively from [243, 233, 234, 230, 239].)

Optical elements with similar transmission functions have been known for several decades under various names, such as 'phase helical filter' [218], 'helical waveplate' [219], or 'Fresnel-type lens filter' [220]. The use of SPPs to form OV beams with OAM was first proposed in 1994 in [221]. Since then, SPPs could be considered the most common optical element for the formation of optical beams.

The azimuthal phase change required to form an OV beam with a TC ℓ can be produced using either an SPP with a monotonic phase increase from 0 to 2π [221] or a sectoral SPP (also called a kinoform element [222]) separated into ℓ azimuthal sectors with the phase varying from 0 to 2π in each of them (Fig. 6a, b). The production of monotonic SPPs becomes a rather difficult task when higher-order OV beams must be formed, because the height of the relief of the optical element increases with increasing ℓ. For example, to form an OV beam with $\ell = 50$ at a wavelength of 532 nm in air, an SFZP must be fabricated from fused quartz with a relief height difference of about 58 μm. This requirement complicates the manufacturing process of SPPs and also limits their use in compact devices. The use of the sectoral SPP design allows fabricating higher-order OV-beam generators whose relief height is not related to their TC, but at the same time requires a higher transverse resolution of the fabrication technology [223–227].

Various technologies have previously been used to fabricate SPPs, including ultraviolet lithography [228], the molding technique [229], electron beam lithography in polymethyl methacrylate (PMMA) [230–232], laser-induced two-photon polymerization [233–237], direct laser recording in combination with plasma etching of a quartz substrate [238], ion-beam lithography [239, 240], mechanical polishing of an olefin polymer [241, 242], and milling of a PMMA sample [243] (Figs 6d–g). In addition, the construction of a very simple SPP from combinations of quarter-wave plates and spaced half-wave plates has been proposed [244]. Such

elements can also be realized in the form of spiral phase mirrors fabricated by photolithography or processing on an ultraprecise lathe with a diamond coating [245, 246]. In the last case, the required phase distribution on the mirror surface is created mechanically using a cutter, and hence the SPP phase profile is superimposed on the wavefront of the incident beam during its reflection. We note that spiral phase mirrors fabricated on an aluminum plate 1 inch in diameter have been used to successfully form an OV beam with TCs up to 5050 [246].

To ensure the best performance of an SPP, its surface profile must change monotonically, which is still a problem for most manufacturing technologies. Discretization of the element profile into a finite number of sectors, each having a fixed height, allows simplifying the fabrication [247]. At the same time, it is obvious that such discretization affects the efficiency of the conversion of the incident radiation into the desired OV beam. It has been shown that a multilevel SPP with $N = 16$ levels can provide a 78% conversion efficiency [247]. An analytic expression describing the scalar theory of Fraunhofer diffraction of a plane wave by an SPP with a multilevel continuous monotonic profile was derived in [248]. The authors showed that, in order to keep the deviation of the conversion efficiency from the optimal one (corresponding to the use of an ideal monotonic SPP) within 2%, the required number of profile discretization steps should be from 19 to 39 for an OV beam with the respective TC from 2 to 10 to be formed. Further studies have shown that, with an even smaller number of steps of a discrete relief, the beam quality deteriorates due to the appearance of OV beams with other values of the TC ℓ [249].

It follows from Eqn (4) that the SPP properties depend on the wavelength of the incident radiation. In accordance with the theory of fractional-order OVs, the wavelength mismatch in the case of an SPP with a monotonic profile changes the profile of the generated intensity distribution, which in this case can be represented by a superposition of two OV beams with adjacent integer TCs [250–255]. In the case of sectoral SPPs, such a mismatch leads to a decomposition of the ℓth-order OV beam into ℓ first-order off-axis OVs [256]. We note that SPPs can also be used to form ultrashort femtosecond OV pulses with a large spectral width: in this case, the use of so-called achromatic SPPs is required [257]. Achromatic SPPs can be realized, for example, by combining two SPPs made of different materials with a helicoid-like interface [258]. The use of a similar design to implement an achromatic SPP with 36 discrete relief steps made it possible to form an OV beam with a mode purity of more than 95% in a spectral bandwidth exceeding 140 nm in the optical range [259].

Typically, SPPs are used to form OV beams with a fixed TC. In 2004, however, a tunable SPP made of a deformed Plexiglas plate with a radial crack was proposed, which allowed forming OV beams with the TC in the range from 1 to 3 [252]. A modified version of the SPP, a radially modulated SPP with an additional phase shift in the radial direction, allowed tuning the TC of the formed OV beam in the range from 2 to 5 by changing the radius of the incident annular beam [260]. Such an element can also operate at different wavelengths to form OV beams with the same TC. Tunable SPPs based on LCs have also been implemented and used to form OV beams with the TC up to 6 and the mode purity exceeding 94% [261, 262]. Finally, it was reported that an element that combines two SPPs with a moiré effect [263] allows tuning the TC of the formed OV beam in the range from 1 to 10 by rotating the plates relative to each other [264]. The transmission function of superimposed elements then corresponds to the transmission function of a single SPP, and the relative rotation angle allows gradually adjusting its TC. The dependence of the SPP properties on the incident radiation wavelength can also be used to change the TC of the formed OVs when a high-relief SPP is illuminated with laser radiation with an adjustable wavelength [265].

Tunable SPPs can also be implemented using adaptive spiral mirrors bent into a helical shape [266]. This allows converting 95% of the incident radiation into an OV beam with the TC tunable in value and sign [267]. Such a spiral mirror can be based on a cheap, compact, and lightweight segmental deformable mirror with a small number of segments. The possibility of using such mirrors to form OV beams with a TC gradually increasing in the range from 0 to 4 was demonstrated in [268]. Moreover, sectoral deformable mirrors, due to their achromatic properties and the possibility of tuning, can be used to form optical beams with a higher mode purity than that of optical beams created by sectoral SPPs.

We note that the unique structure of SPPs allows implementing a femtosecond OV beam generator with a power up to 4.6 TW [269], as well as a variety of unique microscale devices: an OV beam generator based on an SPP integrated into an optical fiber [240], on-chip components capable of wavelength-selective generation of OV beams (so-called vortex microelectromechanical systems, MEMS filters) [233, 236], OV beam generators for optical communication integrated in the output aperture plane of a surface-emitting vertical-cavity laser [239, 270], and optically driven microrotors for applications of microfluidics and 'lab-on-a-chip' devices [271]. SPPs are also used as an intracavity optical element for direct generation of OV beams with a mode purity exceeding 99.9% [272, 273].

6. Spin–orbit interaction for the formation of optical vortices

6.1 Formation of vortex beams using natural anisotropic media

It is known that a uniaxial or biaxial crystal, which is an anisotropic medium with dislocations of optical properties dependent on the light propagation direction, converts circularly polarized input laser radiation into the output optical field with the opposite circular polarization and screw wavefront dislocation. In this case, it is customary to speak of the observation of a spin-orbit interaction, namely, the interaction of the SAM associated with the circular polarization of the incident light and the OAM associated with its spiral wave front.

In 2001, King and collaborators first demonstrated the formation of an OV beam as a result of the conversion of a circularly polarized zeroth-order Bessel beam that passed through a biaxial birefringence crystal [274]. The polarization vectors of the slow and fast modes inside such a crystal can be expressed as

$$\begin{aligned} \mathbf{c}_1(\varphi) &= -\mathrm{i}2^{-1/2}\left[\mathbf{e}_+ \exp\left(\frac{\mathrm{i}\varphi}{2}\right) - \mathbf{e}_- \exp\left(-\frac{\mathrm{i}\varphi}{2}\right)\right], \\ \mathbf{c}_{-1}(\varphi) &= 2^{-1/2}\left[\mathbf{e}_+ \exp\left(\frac{\mathrm{i}\varphi}{2}\right) + \mathbf{e}_- \exp\left(-\frac{\mathrm{i}\varphi}{2}\right)\right], \end{aligned} \tag{5}$$

where φ is the azimuthal angle in polar coordinates, $\mathbf{e}_{\pm} = 2^{-1/2}(\mathbf{e}_1 \pm \mathrm{i}\mathbf{e}_2)$ are the unit vectors for the right and left circular polarizations, and $\mathbf{e}_1$ and $\mathbf{e}_2$ are unit vectors in a Cartesian coordinate system with the z-axis parallel to the crystal binormal. Analyzing the Fourier spectrum of the input field of a birefringent crystal, one can show that the complex amplitude of the light field inside the crystal can be expressed in cylindrical coordinates (ρ, φ, z) as

$$\mathbf{a}(\rho,\varphi,z) = \frac{a_0}{(2\pi)^2}\sum_p \int\int F(q,\varphi_1,z)\alpha_p(\varphi_1)\,\mathbf{c}_p(\varphi_1) \times \exp\left[\mathrm{i}qp\cos(\varphi-\varphi_1) - \mathrm{i}p\beta qz\right] q\,\mathrm{d}q\,\mathrm{d}\varphi_1\,, \quad (6)$$

where $F(q,\varphi_1,z)=F_{\mathrm{in}}(q,\varphi_1)\exp\left[-\mathrm{i}q^2z/(2k)\right]$, $\rho=\left[(x-\beta z)^2+y^2\right]^{1/2}$, $q=(k_x^2+k_y^2)^{1/2}$,

$$\beta = \arctan\left\{\frac{c^2\left[(\varepsilon_3^{-1}-\varepsilon_2^{-1})(\varepsilon_2^{-1}-\varepsilon_1^{-1})\right]^{1/2}}{2v^2}\right\},$$

where β is the crystal anisotropy parameter, k is the wavenumber, k_x and k_y are orthogonal components of the wave vector, α_p are the eigenvalues of the vectors $\mathbf{c}_p(\varphi)$, a_0 is the light field amplitude at the entrance to the crystal, c is the speed of light in a vacuum, v is the phase velocity of the wave, ε_1, ε_2, and ε_3 are principal values of the total permittivity tensor, $F_{\mathrm{in}}(q,\varphi_1)$ is the Fourier spectrum of the field at the input to the crystal, and φ_1 is the angular coordinate in the Fourier spectrum plane.

It can be shown using Eqns (5) and (6) that, for a light field with left/right circular polarization, a superposition of two waves with orthogonal circular polarizations is excited, one of which is in fact an OV beam with the TC $\ell = \pm 1$,

$$\mathbf{a}(\rho,\varphi,z) = \frac{a_0}{2\pi}\int F(q,z)\left[J_0(qp)\,\mathbf{e}_{\mp}\cos(\beta qz) - J_1(qp)\exp(\pm\mathrm{i}\varphi)\mathbf{e}_{\mp}\sin(\beta qz)\right] q\,\mathrm{d}q\,, \quad (7)$$

where J_m is the mth-order Bessel function of the first kind.

For certain values of the crystal length, the crystal anisotropy parameter, and the angle of convergence of the incident Bessel beam to the crystal axis, the conversion of the incident radiation into an OV beam can be implemented with an efficiency close to 100%. In addition, the repeated passage of the formed OV through the crystal can be used to increase its TC.

In 2002, Volyar's group demonstrated that the propagation of a circularly polarized singular beam through a uniaxial crystal is accompanied by the appearance of additional features in the polarization structure of the converted beam. It was found that, when a laser beam passes through a birefringent quarter-wave plate and a polarizer, such features transform into phase singularities [275]. The presented approach can be used to form OV beams with the TC 1 and 2. Later, it was shown that an optical system that combines two uniaxial crystals with perpendicular crystal axes and a polarizer is capable of converting circularly polarized initial radiation into an OV beam for both coherent and incoherent radiation [276]. Expressions for the left and right circularly polarized components of a paraxial beam propagating along the optical axis of a uniaxial crystal are presented in [277], where the authors considered both polarization components as a superposition of arbitrary-order vortex beams and showed that the ℓth-order vortex only affects the $(\ell+2)$th- or $(\ell-2)$th-order vortices of the propagating components with respective right or left circular polarization. This leads to the transformation of the initial circularly polarized beam propagating inside the crystal into an OV beam with orthogonal circular polarization with the TC $\ell = 2$. Then, the second-order OV beam is formed by transforming the projection of the total angular momentum flux on the optical axis of the crystal. The dynamics of such an optical spin-orbit interaction in a uniaxial crystal were studied theoretically and experimentally in [278–280]. It was also found that the efficiency of spin-orbit conversion for Bessel–Gauss beams propagating through a uniaxial birefringent crystal reaches 100%, even for a relatively small crystal length [281, 282]. Due to the spin-orbit transformation, circularly polarized optical fibers focused along an axis of an anisotropic crystal can be used to form beams with cylindrical (radial and azimuthal) polarization [283]. We note that the oblique incidence of circularly polarized radiation on birefringent crystals can lead to the formation of four independent OV beams, which produce a complex field distribution, the so-called vortex four-refraction phenomenon [284–286]. In addition, uniaxial crystals can be used to obtain fractional-TC optical beams with an efficiency up to 95% [287].

OV beam generators based on birefringent crystals are characterized by an almost ideal 100% conversion efficiency and a high destruction threshold, reaching 0.1 TW cm^{-2} [288], as well as the ability to form OV beams in the case of nonmonochromatic light, so-called white light OVs [289–291], in a sufficiently wide spectral range, up to 250 nm [292–294]. In addition, such elements do not require any special high-precision processing technologies to realize a birefringent crystal in the form of an optical microelement.

6.2 Pancharatnam–Berry optical phase element

In addition to using natural crystals, artificial crystals can also be produced that exhibit birefringent properties to be used to form OV beams. For example, a Pancharatnam–Berry optical phase element, which is a special configuration of subwavelength periodic structures (nanogratings), acts as a uniaxial birefringent crystal with optical axes parallel and perpendicular to the orientation of these subwavelength structures [295, 296]. The Pancharatnam–Berry phase, also called geometric or topological, is the one that occurs as the polarization changes in space and can be illustrated using a Poincaré sphere (Fig. 7a). A Pancharatnam–Berry optical element (PBOE) works like a wave plate with a constant delay and continuously changing fast axes with the orientation determined by the angle $\theta(x,y)$. The initial circularly polarized laser beam (the north and south poles of the Poincaré sphere in Fig. 7a) passes along different paths over the Poincaré sphere. These paths lead to spatially noninvariant modifications of the wavefront that arise from the local geometric phase $\varphi_p(x,y) = \pm\theta(x,y) \mp \arctan(\sin 2\chi \tan\theta) = \mp\Omega/2$ (where Ω is the angle of the geodesic triangle formed by the polarization states under consideration, and the angle χ specifies the ellipticity of the generated laser beam). Thus, the orientation of the grating, determined by the spatially varying grating vector $\mathbf{K}_{\mathrm{g}}(x,y)$, can be used to control the phase profile of the initial beam (Fig. 7b).

The formation of OV beams using a PBOE with a helical geometric phase, the so-called helical PBOE, was first demonstrated by Biner et al. [297] in 2002. The proposed helical PBOE that formed an OV beam in the IR range (at a wavelength of 10.6 μm) with the TC $\ell \leqslant 4$ was a subwavelength grating made by photolithography with the direction

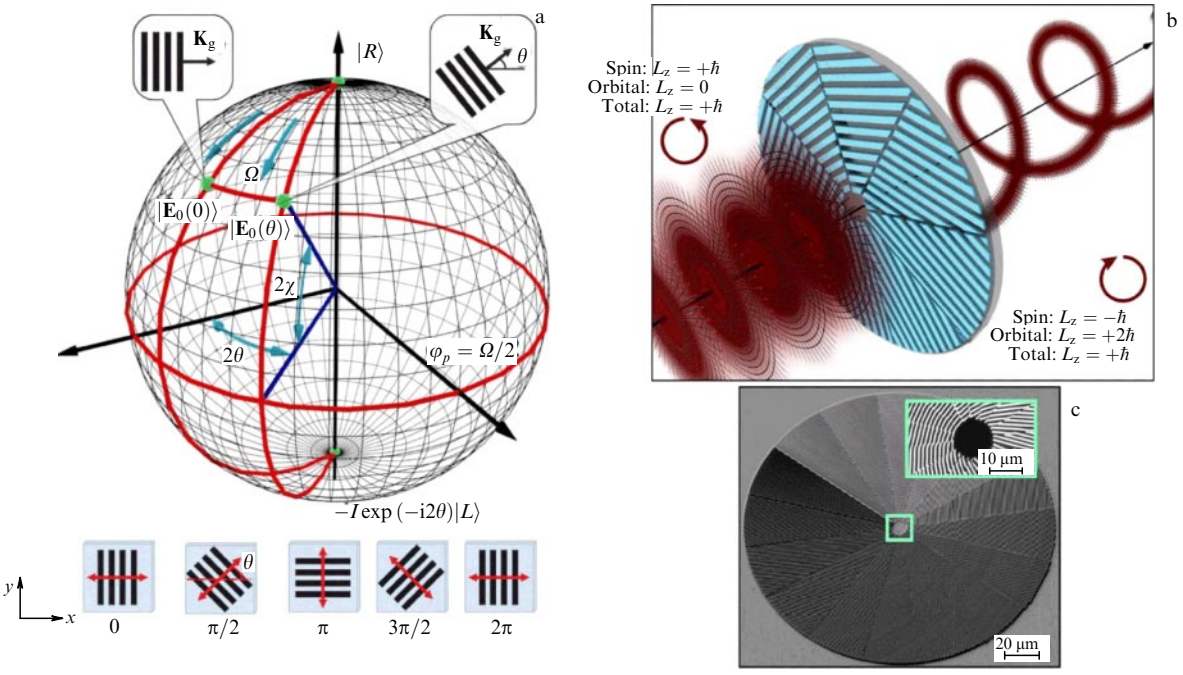

Figure 7. (Color online.) (a) Illustration of the principle of spin-orbit interaction using a Poincaré sphere. Light with right-hand circular polarization is incident on a wave plate with a constant phase delay and the fast axis continuously changing in space, its orientation determined by the angle θ. Because the direction of the fast axis changes in space, the light beam has different trajectories over the Poincaré sphere at different points, which leads to local changes in the phase front due to the geometric (Pancharatnam–Berry) phase. (b) Schematic representation of the principle of OV generation using a PBOE, illustrating the conservation of the total angular momentum of photons as a result of the transformation of a circularly polarized (SAM $= +\hbar$) Gaussian beam with zero OAM into an OV with a helical wave front (OAM $= 2\hbar$) and an oppositely directed circular polarization (SAM $= -\hbar$). (c) SEM image of an optical element in the form of spatially varying subwavelength gratings (PBOE) with the fast axis oriented at different angles $\theta(x, y)$, and corresponding Pancharatnam–Berry geometric phase values. (Figures a and b from [296], figure c from [303].)

of the grooves constantly changing in space by an angle defined as $\theta(r, \varphi) = \ell\varphi/2$ in polar coordinates (Fig. 7b). Implemented for the near and mid-IR ranges, PBOEs provide a rather high efficiency of the incident beam conversion into OVs, reaching 98% [298–300]. In moving to the optical range, the characteristic periods of the spatial arrangement and sizes of nanograting grooves are to be scaled appropriately (the characteristic groove size must be an order of magnitude smaller than the wavelength), which significantly complicates the practical implementation of optical elements based on them. At present, extremely expensive and poorly scalable methods of electron and ion-beam lithography remain the main approaches for the fabrication of highly efficient PBOEs with a resolution of at least 100 nm. At the same time, we note attempts to use high-performance laser fabrication methods: laser-induced multiphoton photopolymerization and direct laser ablation of thin metal films for the production of PBOEs for the optical spectral range [303, 304]. An example of such a PBOE formed by nanogratings photopolymerized on the surface of a quartz substrate, intended for the generation of OVs with a TC equal to 1, is shown in Fig. 7c. The potential of the two-photon photopolymerization method was also demonstrated in [303] using the example of a PBOE for the generation of optical fibers with a TC up to 20.

6.3 *q*-wave plates

In 2006, Marrucci et al. [305] demonstrated a PBOE given by a thin LC film fixed between two glass slides (Fig. 8a), which allowed forming OV beams in the optical range. The authors of [305] presented a new type of PBOE profile, given as $\theta(r, \varphi) = q\varphi + \theta_0$, where $q = 0, \pm 1/2, \pm 1, \ldots$ is a number that changes with a half-integer step and determines the TC of the optical element as $\ell = 2q$, and θ_0 is a constant equivalent to the value of the initial rotation of all vectors of spatially noninvariant subwavelength gratings that form this element. Such an optical element, called a q-plate, introduces local modulations $\pm 2q\varphi$ into the wavefront of the incident plane wave, thereby allowing the formation of an OV beam with the TC $\ell = 2q$. The Jones matrix that describes the transformation of a field passed through a q-plate has the form

$$M(\varphi) = \begin{pmatrix} \cos(2q\varphi) & \sin(2q\varphi) \\ \sin(2q\varphi) & -\cos(2q\varphi) \end{pmatrix}. \quad (8)$$

After passing through the q-plate with a phase delay π characteristic of half-wave plates, each circularly polarized photon reverses its polarization, which leads to a change in the z-component of the SAM from $\pm\hbar$ to $\mp\hbar$. The q-plate with $q = 1$ then acts just as an optical SAM-to-OAM converter: the z-component of the OAM of each photon changes from 0 to $\pm 2\hbar$, and hence the total change in the angular momentum of light is zero (Fig. 7b) [306, 307]. Calculating Fresnel's scalar propagator for a laser beam incident along the normal on a q-plate surface element with $q = 1$ shows the possibility of achieving a conversion efficiency close to 100% [308]. We note that, as in the case of holograms or SPPs, the TC $\ell = 2q$ of the formed OV beam can easily be increased by using a cascade of several q-plates located immediately one after another [305].

Various approaches have been used to fabricate q-plates, including the formation of the required orientation profile of LC cells using circular grinding [308], microscale grinding

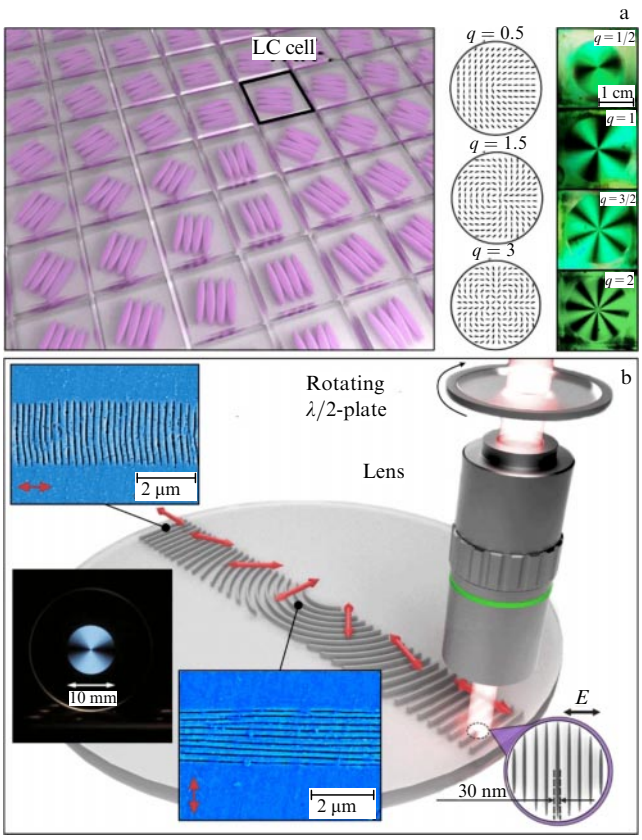

Figure 8. (Color online.) (a) Schematic representation of a piece of a q-plate consisting of LC cells with a specific crystal orientation profile in each cell. Right-hand side of the figure shows examples of q-plate profiles with $q = 0.5$ and 1 and an optical image (in crossed polarizers) of corresponding LC q-plates controlled by an external electric field. Lines on the profiles of the q-plates indicate the orientation of the local subwavelength gratings in the transverse plane. (b) Schematic representation of the process of producing anisotropic nanogratings formed inside a transparent material using direct femtosecond laser recording. Local orientation of the nanogratings is controlled by rotating the polarization direction of incident laser radiation (shown schematically by red arrows). Insets show SEM images of self-organizing nanogratings formed inside quartz glass when it is scanned along the x-axis by femtosecond laser pulses linearly polarized along or across the scanning direction. (Figure a from [307, 320], figure b from [348, 330].)

[309], reverse grinding [310], and illumination of the LC layer with photomasks or holographically formed beams [311] or using the sample photopolymerization procedure with a spatially controlled scanning laser beam [312]. However, these methods do not allow realizing the dynamical rearrangement of the structure of q-plates for the controlled formation of OV beams at different wavelengths. To overcome this limitation, tunable q-plates with an optical phase delay controlled by thermal heating [313] or an external electric field [314–316] have been proposed. In particular, an external electric field can be used to create tunable LC q-plates with a switching time of 25–30 ms [315] and, in addition, to create q-plates that are tunable in terms of not only the radiation wavelength [317] but also the TC of the formed OV beam [318]. Faster switching (with a switching time up to 75 μs) of the formation of OV beams with opposite TCs is also possible when using static q-plates in combination with an electrically controlled uniformly oriented ferroelectric LC [319].

Due to their properties, q-plates have found application in many areas of modern science [320–326], including the formation of an arbitrary vector laser beam of an arbitrary order directly from a laser cavity [327]. A detailed review of the principles of the implementation of q-plates and their recent applications can be found in [328].

To conclude this section, we note that the concept of a generalized q-plate described by the Jones matrix

$$M(\varphi) = \begin{pmatrix} \cos\left(2\Phi(\varphi)\right) & \sin\left(2\Phi(\varphi)\right) \\ \sin\left(2\Phi(\varphi)\right) & -\cos\left(2\Phi(\varphi)\right) \end{pmatrix} \tag{9}$$

with an arbitrary continuous periodic function $\Phi(\varphi)$ was introduced in 2019 [329]. A wider choice of the function $\Phi(\varphi)$ and the possibility of implementation using, for example, SLMs make the generalized q-wave plate an optical element with great potential for the formation of vector OV beams.

6.4 S-wave plates: q-plates formed inside transparent dielectric materials

Structures exhibiting the birefringence effect, which underlies the formation of OV beams with the help of crystals, can be artificially created not only on the surface but also in the bulk of transparent materials. In particular, such birefringent structures can be formed due to self-organization induced by ultrashort linearly polarized laser pulses focused in the bulk of dielectric materials [330]. When the energy density of an incident laser pulse exceeds a certain threshold, nonlinear absorption of light occurs inside a transparent dielectric material, which leads to its irreversible modification due to the formation of structural defects [331], a local change in the refractive index [332], or the appearance of nanocavities [333].

In 1999, unusual anisotropic polarization-dependent light scattering was demonstrated, observed from micrometer-size modified regions formed by femtosecond laser pulses inside germanium-doped quartz glass [334]. Later, this phenomenon was explained by the formation of a self-organizing nanograting in the irradiated focal volume, with the grooves oriented in a direction strictly perpendicular to the polarization direction of the incident laser radiation [335].

The formation of a nanograting is associated with the appearance of a photoexcited material with a periodically modulated intensity profile in the focal volume; this is caused by the interference of incident laser radiation scattered by a locally generated plasma. Subsequently, it was found that the nanograting period can be controlled by both the number and energy of laser pulses irradiating a selected area. Rotation of the polarization direction of pulses focused in the bulk of a transparent material can be used to control the spatial orientation of the formed nanogratings (shown schematically in Fig. 8b), with the laser beam scanning creating areas with specified birefringent properties inside the dielectric material [336]. In 2011, Kazansky's group presented a spatially noninvariant half-wave plate fabricated by direct laser recording of self-organizing nanogratings inside quartz glass [337]. Such self-organizing nanogratings can be regarded as birefringent crystals with the respective slow and fast optical axes oriented parallel and perpendicular to the grating groove direction. Such an element (also called an S-wave plate or a Southampton-super-structured waveplate; see the inset to Fig. 8b) can be used to transform an incident linearly polarized Gaussian beam into a beam with an annular intensity profile and a radial or azimuthal distribution of the profile polarization depending on the orientation of the linear polarization of the incident radiation relative to

the optical element axis. When illuminated by a circularly polarized laser beam, the S-wave plate converts it into an OV with the opposite circular polarization and the TC $\ell = 1$ [337–339], as in the case of a q-plate with $q = 1/2$.

The technology of direct femtosecond laser recording of birefringent structures in the form of nanogratings has been implemented in various crystalline materials, such as sapphire [340] and TeO_2 [341, 342], and also in pure quartz [343], titanium silicate [344, 345], and borosilicate [344, 346] and alkali-free aluminoborosilicate glasses [347]. A typical threshold value required for the irreversible modification of a transparent material via the formation of a self-organizing nanograting is approximately 1 TW cm^{-2} [347], and therefore sufficiently powerful OV beams can be formed using such an element. The TC of the generated OV beam can also be increased using a cascade of S-wave plates. We note that an S-wave plate for the formation of an OV beam with the TC $\ell = \pm 100$ was recently demonstrated [348]. At the same time, the presented estimates based on direct laser recording methods suggest the possibility of manufacturing plates with a diameter of at least 10 mm for the formation of OV beams with a TC up to 10,000.

We note that spatially varying self-organizing nanogratings recorded inside a transparent material can have a sufficiently high transmittance, which is mainly affected by scattering losses. For example, an S-wave quartz glass plate has a transmission of more than 80% in the optical range and about 95% in the near-IR range. Standard S-wave plates work efficiently in a rather narrow spectral range (± 20 nm from the central wavelength). However, a polarization-selective filtering technique has been developed to extend the spectral bandwidth of S-wave plates using a filter that combines an achromatic quarter-wave plate and a linear polarizer. This approach allowed an S-wave plate fabricated for a wavelength of 530 nm to be used to form OV beams in the entire optical and near-IR ranges (with a spectral band of about 600 nm) with the conversion efficiency exceeding 50% [349].

The production of S-wave plates using femtosecond laser recording is a patented commercialized technology (EU Femtoprint project) with a number of applications in various fields of science and industry. The ease of use of these optical elements and their integration into various optical systems, combined with a high laser damage threshold and high transmittance, have made them very popular in laser material processing (see also Section 10). Such optical elements have found application in problems concerning the formation of coherent vector beams in the extreme ultraviolet range [350] and in superresolution optical microscopy [349]. In addition, S-waveplates allow tuning the total OAM of the formed OV beam in a range from 0 to $\hbar$ per photon by changing the incident beam polarization from circular to elliptical and linear. This possibility provides a convenient tool for controlling the rotational motion of various particles and biological objects (for example, DNA) captured by the formed OV beam [348, 351].

6.5 Microscale generators of optical vortices based on topological defects

Optical elements in the form of q-plates and S-wave plates are rather bulky, which does not allow their use in integrated optics devices. In 2009, a microscale generator of OV beams based on a droplet of birefringent liquid several micrometers in diameter was presented [352]. As a result of the addition of a surfactant (cetyltrimethylammonium bromide, CTAB) to a spherical droplet containing nematic 5CB LCs, both the director, which is an axial unit vector that determines the local directions of the long axes of molecules, and the local optical axes inside the droplet acquire a three-dimensional spherically symmetric spatial distribution. Such a spatial conformation of optical axes determines inhomogeneous birefringence with a defect at the center of the droplet, with the director rotated through 2π about it. Optical beams with a spiral wavefront also form when using such a 'radial' droplet due to the geometric phase that arises in this case due to continuous transverse changes in the radial distribution of the optical axis with the same initial and final states. The approach under consideration ensures the controlled formation of microscale OV beams with a variable TC and an efficiency reaching 40%, depending on the droplet diameter. The use of electrically controlled topological defects (so-called umbilical points, or umbilics) in nematic LC films allowed implementing the tunable generation of OV beams [353–356] and also led to the creation of a class of umbilical q-plates [357, 358]. We refer the interested reader to review [359], where the mechanism of formation of OV beams using umbilics in LC media is described in detail.

Topological defects in the form of voids or bubbles inserted into an isotropic transparent medium with a relatively high refractive index contrast are known to exhibit edge birefringence associated with different transmissions of s- and p-polarized waves [360]. In 2011, it was theoretically and experimentally shown that, on spherical microvoids formed inside glass under irradiation with femtosecond laser pulses, the initial circularly polarized light is converted into a second-order OV beam with reversed circular polarization [361]. Thus, topological defects provide a reliable way to implement highly efficient controllable OV beam generators at the microscale. In particular, such devices allowing spin-orbit interaction of light to be localized within a few micrometers can be of interest in areas such as the optical capture/rotation of micrometer and submicrometer particles [362–364].

7. Plasmon generators of optical vortices

It is well known that, under certain conditions, electromagnetic radiation incident on a dielectric–conductor interface (with a noble metal typically acting as the conductor) can be converted into a hybrid type of surface electromagnetic wave (so-called surface plasmon–polariton waves, SPPWs) [365]. However, an electromagnetic wave cannot be directly converted into an SPPW under normal incidence on a smooth metal surface due to a mismatch in the wave vectors. A number of approaches have been developed that allow implementing such a transformation using various nanoantennas (in the form of nanoslits, nanoholes, or nanotips), prisms, or input gratings. In addition to that transformation, nanoantennas arranged in a special way on a metal surface allow focusing SPPWs, which can be used to implement nanosize focusing elements for plasmon waves [366–369].

In 2008, Gorodetski et al. [370] demonstrated a plasmon microlens that can effectively convert a normally incident circularly polarized electromagnetic wave into SPPWs converging at the center of the microlens and forming an OV. For the conversion and subsequent focusing of SPPWs, the authors of [370] proposed an original design of a microlens made of spirally oriented nanogrooves engraved on the

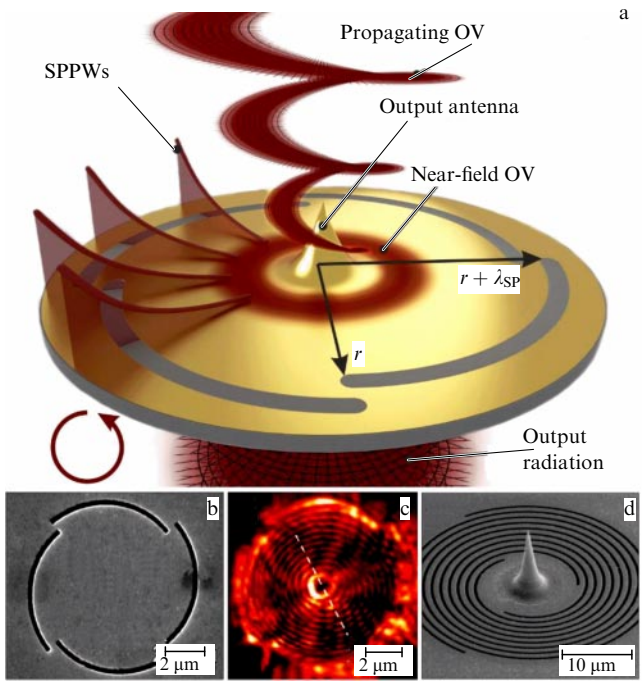

Figure 9. (Color online.) Plasmonic generators of OV beams. (a) Schematic representation of the principle of operation of a plasmonic microlens designed to generate and output into free space an OV beam formed at the center of the microlens by converging SPPWs excited by helical nanoslits. Cone-shaped nanotip transforms the plasmonic OV localized on the surface into an electromagnetic wave propagating into free space. (b, c) SEM image and near-field optical image of a plasmonic microlens generating an OV in the plane of a metal film. (d) SEM image of a plasmonic microlens allowing the plasmon vortex to exit into free space. (Figures b and c from [372], figure d from [381].)

surface of a thick gold film by ion-beam lithography. A similar design was realized somewhat later in [371], where, for more efficient excitation and focusing of SPPWs, nanoslits were used instead of nanogrooves, located along a spiral trajectory

$$r_\ell(\varphi) = r_i + \frac{\lambda_{SP} \bmod (\ell\varphi, 2\pi)}{2\pi}, \qquad (10)$$

where mod (...) is the remainder of integer division, λ_{SP} is the surface plasmon wavelength, ℓ is the TC of the plasmonic OV, r_i is the shortest distance from the center of the microlens to the nanoslit, and $r_0 = r_i + \lambda_{SP}$ is the maximum distance from the center of the microlens to the same nanoslit (Fig. 9a). The general principle of operation of such plasmonic microlenses is based on the creation of a specially designed nanorelief on the surface of a noble metal, ensuring the excitation of SPPWs converging toward the center of the microlens. The structures forming the nanorelief are located along a spiral trajectory relative to the center of the microlens, thereby providing the corresponding phase shift for the plasmon waves that converge to the center and forming the OV. The concept developed subsequently became widely used, including for the implementation of planar plasmonic elements for the formation of plasmonic OVs with a fractional TC [372–376]. Progress in this area has led to the creation of alternative designs of plasmonic microlenses that can generate OVs when pumped by linearly polarized radiation [377, 378].

We note that SPPWs exist at the metal–dielectric interface and do not propagate into free space without the use of additional methods and cannot therefore be detected by classical optical methods. To visualize plasmonic OVs, near-field optical microscopy methods are often used, with the distribution of the electromagnetic field amplitude in the plane of a metal film scanned by a nanosize optical probe. An example of such a visualization of a microsize plasmon OV focused by the spiral plasmonic microlens described above is shown in Fig. 9c. The use of nanoantennas allows not only efficient conversion of the incident radiation into SPPWs but also reverse conversion, i.e., the output of electromagnetic waves localized at the metal–dielectric interface into free space (Fig. 9a). This concept was implemented in the example of a similar helical plasmon microlens produced on both surfaces of a metal membrane, in the center of which a nanoantenna was formed by a through nanohole in order to output the generated OV into free space [379, 380]. To increase the efficiency of conversion of a near-field OV into a propagating OV beam, a single-layer plasmonic lens with a nanoantenna in the form of a cone-shaped nanotip was later proposed [381, 382]; a scanning electron microscope (SEM) image of the lens is shown in Fig. 9d.

Plasmonic lenses for OV generation are characterized by a relatively low laser damage threshold and a conversion efficiency of several percent, and are also quite expensive to manufacture; therefore, the practical necessity of creating such optical elements for generating optical fibers raises doubts. On the other hand, SPPWs can have a wavelength much shorter than that of an electromagnetic wave propagating in free space, and the focusing of SPPWs is not limited by the fundamental Abbe diffraction limit. From this standpoint, the development of plasmonic OV generators can be regarded as a first attempt to obtain singular light localized on a nanoscale [383–386]. In addition, the planar geometry of plasmonic elements of microoptics is an extremely convenient platform for fundamental studies of electromagnetic waves localized on subwavelength scales, including problems of their spatiotemporal evolution and spin-orbit conversion [387].

8. Formation of optical vortices using metasurfaces

Metasurfaces are a special class of nanomaterial made of specially designed and organized nanoscale structures (nanoantennas or meta-atoms) on a substrate surface that allow implementing various ultrathin optical elements (focusing lenses and axicons) [388], holograms [389, 390], quarter-wave plates [391], and OV generators [392]. Several reviews devoted to this extremely popular research subject are currently available [393–396], and we therefore restrict ourselves in this section to the main principles of operation of metasurfaces for the formation of OVs, focusing on their advantages and disadvantages in comparison with other types of OV generators.

When using metasurfaces, the phase shift required to transform the initial electromagnetic wave into an OV is achieved due to nanosize structures, each of which can be considered a local source of scattered electromagnetic waves. In the general case, the phase shift provided by a nanoantenna is determined by its geometric shape and orientation (relative to the polarization of the incident radiation), which allows a high-accuracy modulation of the wavefront of an electromagnetic wave reflected from or transmitted through the metasurface (Fig. 10a). The first metasurfaces for controlling the wave front of electromagnetic waves were based on

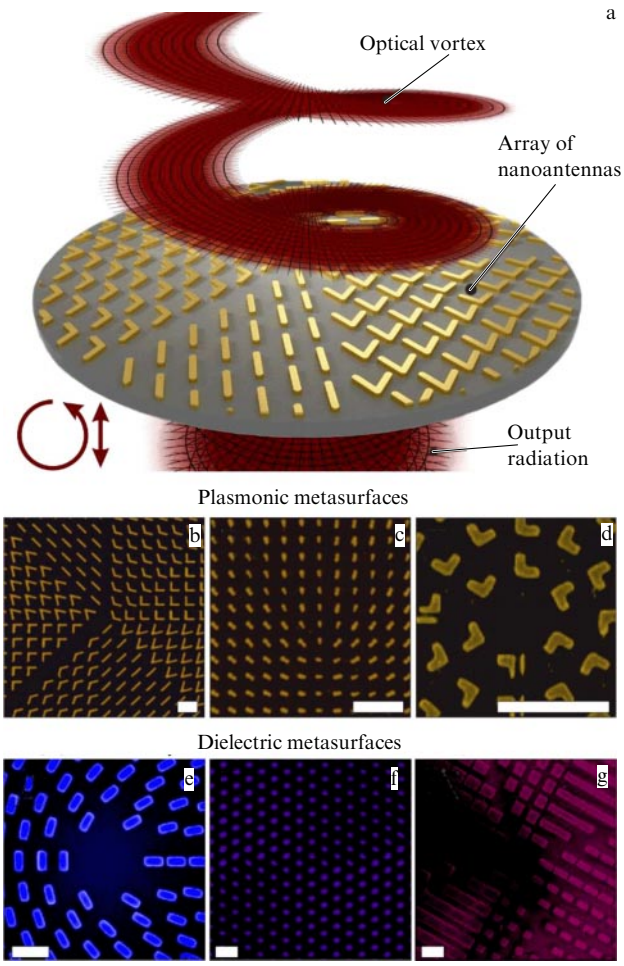

Figure 10. (Color online.) (a) Schematic illustration of the transformation of an incident linearly or circularly polarized Gaussian beam into an OV using a metasurface formed by an array of V-shaped plasmonic nanoantennas. SEM images of parts of metasurfaces formed by plasmonic and dielectric nanoantennas, illustrating the variety of designs for implementing OV generators: (b) V-shaped gold nanoantennas, (c) gold nanorods, (d) L-shaped gold nanoantennas, (e) titanium dioxide nanopillars, (f) elliptical silicon nanopillars, and (g) silicon nanoblocks. Scale bars in all images are 1 μm. (Figures b–g are adapted, respectively, from [392, 400, 399, 418, 412, 413].)

nanostructures made of noble metals that support coherent electron density oscillations induced by the incident electromagnetic field (so-called localized plasmon resonance). It is noteworthy that such electron plasma oscillations in nanostructures can be described with sufficient accuracy using the formalism of a Lorentz oscillator whose oscillations can cover the phase tuning range from 0 to π due to a change in geometry. Thus, to implement an OV generator based on plasmonic nanoantennas, which requires covering the full range of phase from 0 to 2π, the principle of geometric phase (spin-orbit conversion), implemented in PBOE-type elements, must be used. Examples of such devices [397, 398] operating in the mid-IR, near-IR, and optical spectral ranges are shown in Figs 10b–d. To date, various configurations of plasmonic nanoantennas arranged into metasurfaces have been developed that allow efficient control of the incident radiation wavefront; their implementation in the form of various optical elements, including OV generators operating for transmission and reflection, has been demonstrated [401–410].

We note that plasmonic nanostructures have a rather weak scattering intensity in the forward direction. In the optical spectral range, at the same time, noble metals, which are the main building material for the formation of nanoantennas, have significant ohmic losses, reducing the conversion efficiency of OV generators based on them. Obviously, these factors have led to the development of alternative approaches to the design of nanoantennas, among which the use of optically resonant nanostructures made of materials with a high refractive index and low losses has become mainstream [411]. In the optical and near-IR spectral regions, materials widely used for the implementation of nanoantennas include common semiconductors such as Si, Ge, GaAs, and TiO_2 [412, 413]. Nanostructures made from these materials support so-called Mie resonances of an electrical and magnetic nature [414]. The geometry of nanostructures allows controlling the spectral position and intensity of resonances of both types. The spectral match or mismatch of resonances of different natures provides additional capabilities of controlling the radiation pattern of nanoantennas, which can be used to completely suppress waves scattered in a certain direction (Huygens metasurface) [415]. We note that such broad capabilities of controlling the wavefront of an electromagnetic wave in the optical range cannot be realized using plasmonic nanoantennas [416, 417].

The examples of metasurfaces used for the formation of optical fibers based on silicon and titanium dioxide nanoantennas of various geometries shown in Figs 10e–g indicate a similarity between the main concepts and designs of optical elements implemented using plasmonic and dielectric nanostructures. At the same time, moving from metallic to dielectric (semiconductor) materials in the fabrication of nanostructures for the optical spectral range allows the efficiency of the conversion of incident radiation into OVs to be increased by an order of magnitude [412, 413, 418]. For example, an experimentally realized element based on an array of titanium dioxide nanopillars (Fig. 10e) demonstrated a conversion efficiency of 40% to 70% in the entire optical range [418, 419]. The ability of metasurfaces to simultaneously control both the phase and polarization of the electromagnetic waves they generate was used to implement *J*-wave plates — unique optical elements that can convert the SAM associated with the circular polarization of the incident radiation into arbitrary states of the total angular momentum (typically denoted by J) given by the sum of the SAM and OAM [420, 421]. Thus, *J*-plates can be used to eliminate the restrictions inherent in geometric phase elements (Pancharatnam–Berry elements) that transform an initial laser beam with a SAM into a laser beam with opposite SAM and OAM values in accordance with the momentum conservation law (see Section 6). As in the case of other elements used to form OV beams, *J*-plates can be placed inside a laser cavity to directly generate OV beams with a TC up to 100 and mode purity close to 100% [422, 423], and their cascades can be used to form vector vortex beams with different configurations of the total angular momentum [424]. Also, the use of combinations of several quarter-wave plates and two SLMs made it possible to implement a dynamic *J*-plate [425].

Metasurfaces, despite their compactness (optical elements can be formed by a monolayer of nanoantennas with a thickness reaching 100 nm), provide an unprecedentedly high accuracy in controlling the wavefront of electromagnetic waves on subwavelength scales. The compactness of metasurfaces ensures ease of integrating and matching them

with various miniature optoelectronic devices, such as microlasers [419]. This makes practical realizations possible for tunable vortex microlasers, which are promising elements for new-generation optical data transmission systems. Electron-beam lithography provides a standard resolution of about 10 nm in manufacturing individual nanoantennas and their ordered arrays, generally meeting the requirements for metasurfaces in the optical spectral range. At the same time, the search for more efficient and cost-effective methods for the production of metasurfaces, so as to accelerate the production of optical elements and reduce costs while maintaining the possibility of a scalable increase in their lateral size, remains a key task in this field. Among the new promising commercial nanofabrication technologies, we can single out an approach adapted to the problems of texturing large areas with the use of atomic force microscopy with special cantilevers heated to a temperature of 700 °C (see recent review [426]).

To conclude this section, we note that the radiation absorbed by plasmonic nanoantennas is effectively converted into heat, which explains the relatively low damage threshold of elements based on metasurfaces forming OV beams in the optical spectral range. For pulsed laser radiation, the absorbed energy density required for the irreversible modification of a gold film 50 nm in thickness placed on a glass substrate is only 30 mJ cm^{-2} [427]. Moreover, localization and amplification of laser radiation near subwavelength nanostructures (due to localized plasmon resonances in particular) are expected to decrease the irreversible modification threshold by at least another order of magnitude (see, e.g., [428, 429]). Dielectric (semiconductor) nanostructures have lower losses, which allows them, in principle, to withstand a higher power of incident laser radiation. But when magnetic-type resonances are excited in them, such structures can be resonantly heated even more efficiently than their plasmonic nanoantennas due to a significant concentration of the electromagnetic energy inside such nanocavities [430].

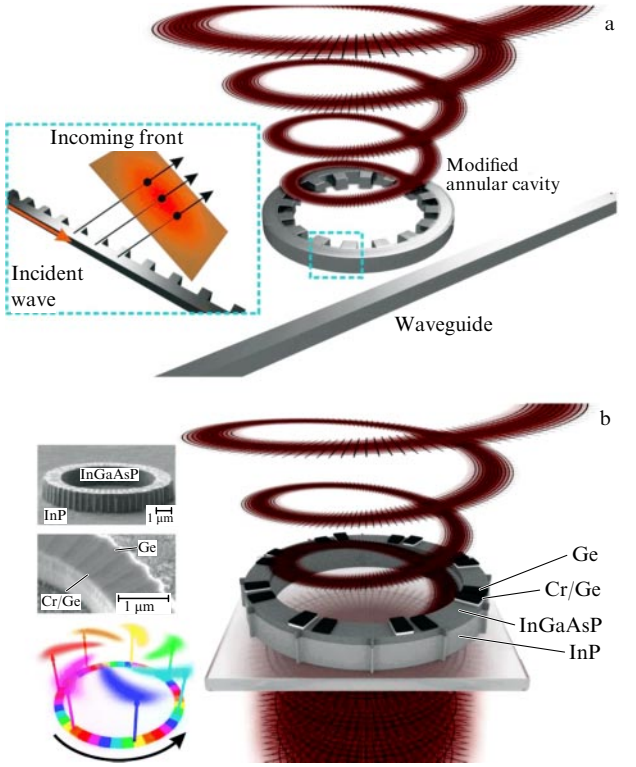

Figure 11. (Color online.) (a) Schematic representation of an integrated OV beam generator formed by a microcavity with an output grating located along its inner wall. Inset shows the formation of an oblique wavefront with the help of an output grating (taken from [438]). (b) Schematic representation of a microlaser on an indium phosphide (InP) substrate generating OV beams at telecommunication wavelengths. Single-layer germanium (Ge) structures with a thickness of 13 nm and double-layer chromium-germanium (Cr/Ge) structures (corresponding to thicknesses of 11 and 5 nm) are periodically located in the azimuthal direction on the upper plane of the InGaAsP/InP microcavity, simulating the modulation of the refractive index and the gain/loss coefficient of selective WGW generation propagating only in one direction (clockwise or counterclockwise). Equidistant protrusions on the outer wall of the microcavity play the role of an output grating. Insets show SEM images of the fabricated microlaser (taken from [451]).

9. Integrated optical generators of optical vortices and vortex microlasers

Numerous studies have recently been devoted to the development of miniature integrated optical devices for the formation of OV beams with intended applications to optical and quantum information transmission and processing systems [431–437]. In 2010, the first experimental implementation of an integrated photonic OV generator was demonstrated, made of an annular cavity, a waveguide, and an array of nanorods [435]. The TC of the OV generated by that device is determined by the difference between the order of a whispering-gallery wave (WGW) excited in the annular cavity and the number of nanorods that scatter it. A year later, another configuration of an integrated optical circuit (IOC) based on a silicon-on-insulator type waveguide was proposed, which allowed generating a focused azimuthally or radially polarized output beam emitted directly from the substrate surface [436].

In 2012, Cai and collaborators demonstrated a microsize OV generator (about 4 μm in diameter) integrated on a silicon substrate and formed by a waveguide and an annular microcavity with periodic modulation of the refractive index in the azimuthal direction (Fig. 11a) [438]. The modulation of the refractive index in this cavity was provided by a diffraction grating located on its inner circumference, which converts and outputs the WGWs into free space in the vertical direction in the form of an OV beam. We note that the WGWs supported by such a cavity have discrete azimuthal propagation constants $v_{\mathrm{WGW}} = \beta_{\mathrm{rad}} R = p$. The integer p is the azimuthal mode number and physically represents the number of optical periods around the cavity, R is the effective WGW radius, and β_{rad} is the light propagation constant for this radius [439, 440]. The elements of the diffraction grating scatter the WGW, and part of the power is deflected in the direction determined by the angle φ at which constructive interference occurs. The wavefront of such emitted light is a plane tilted at the angle φ (see the inset to Fig. 11a). For a waveguide with a grating bent into a loop, the resulting wavefront of the emitted light has a helical shape, which leads to the appearance of an OAM mode propagating in the vertical direction. Under resonant excitation of a microannular cavity, the device is capable of emitting a propagating OAM mode with the TC $\ell = p - q$, where q is the number of scattering array elements placed along the cavity [441]. More complex tilted configurations of scattering elements on the surface of a microannular cavity can be used to radiate a superposition of two OAM states with orthogonal circular polarizations into free space and perform their

subsequent filtering [442]. The conversion efficiency of such OV generators, defined as the ratio of the radiated power of the desired OAM mode to the optical power in the waveguide, ranges from 5 to 37% [443].

The development of similar IOCs for OV generation, implemented by several research groups [444–450], eventually made it possible to develop the concept of an integrated OV microlaser supporting single-mode generation of an OV beam at telecommunication wavelengths with external optical pumping [451]. The device developed was a similar annular microcavity based on WGWs excited by external (nonwaveguide) pumping by a laser beam (Fig. 11b). In this case, due to the mirror symmetry of the annular cavity, the proper WGWs propagating clockwise and counterclockwise can be excited simultaneously, leading to zero total angular momentum of the system. The selection of a WGW propagating in only one direction was achieved due to the original asymmetric modulation of the refractive index and the gain/loss factor along the upper plane of the annular microcavity. In this case, the OV associated with a given WGW is output vertically into free space by means of a periodically modulated outer wall of the microannular cavity, similarly to how this was done in the previously proposed approaches. We note that an integrated OV microlaser with electrical pumping has recently been realized [452].

The concept of a vortex microlaser with the possibility of dynamically tuning the TC of the generated OV beam at room temperature (with attainable TC values of -2, -1, 0, $+1$, and $+2$), implemented in 2020, is based on a combination of the microannular cavity considered above realized on a semiconductor substrate with a 200-nm layer of InGaAsP quantum dots and a waveguide with a 'common bus' topology with two arms for controlled optical pumping and mirror symmetry breaking of the generation of oppositely directed WGWs [453]. Pumping one of the waveguide arms leads to an increase in the generation of one of the WGWs excited in the cavity and an increase in the losses of the oppositely directed WGW. The OV beam is generated at a telecommunication wavelength of 1492.6 nm, and the TC tuning time (including fractional values [454]) of the OV beam is limited only by the optical response of semiconductor quantum dots, i.e., has the potential to achieve ultrafast switching on the picosecond scale, which significantly exceeds the millisecond and microsecond switching times realized with thermooptical control [455]. The technology of selective optical pumping was also used in the implementation of a surface-emitting vortex microlaser with a vertical cavity, based on a spin-polarized active medium: in that case, the rotation direction of the generated helical wavefront is controlled by the type of circular polarization of the pump radiation [456]. However, it is possible to achieve selective WGW generation without amplification/attenuation of losses of one of the modes, but only by using azimuthal spatiotemporal modulation of the dielectric permittivity of a microannular cavity created by a propagating wave grating [457]. This approach also provides a high quality factor (over 20,000), but requires miniature electrical contacts to be connected to the cavity.

Modern computational capabilities make various global optimization algorithms possible, such as combinations of annealing simulation algorithms with genetic algorithms associated with three-dimensional finite-difference time-domain modeling, which opens up prospects for calculating more complex IOC designs with vortex lasers emitting in a fairly wide range of telecommunication wavelengths, from 1450 to 1650 nm, with a 35% radiation generation efficiency and modal purity greater than 97% [458]. Such devices are an ideal means to further increase the throughput of tunable optical communication systems operating at wavelengths in the near-IR range.

Of certain practical interest is also the implementation of vortex microlasers emitting in the optical spectral range. Such microlasers have recently been implemented on the basis of the standard architecture of a vertically emitting active-medium cavity (based on an organic polymer material or lead–halide methyl-ammonium perovskite) combined with a passive OV generator based on an Archimedean spiral grating [459–462]. Another promising class of planar vortex microlasers can be produced on the basis of a cavity that supports so-called continuum bound states (CBSs)—high-Q modes that allow achieving colossal Q-factors, exceeding 10^9 [463]. A vortex CBS-mode microlaser was recently implemented on the basis of a thin lead–halide perovskite film perforated with periodically arranged pass-through nanoholes, resulting in the formation of a Pancharatnam–Berry geometric phase [464–466].

In 2013, Williams and collaborators showed that the phase structure of the light field required for the formation of an OV beam can be directly obtained by using arrays of molecular chromophores that have a certain symmetry and satisfy certain geometric constraints [467, 468]. This type of light emission is a direct result of the electron relaxation of the state of a delocalized exciton supported by an array of at least three chromophores arranged symmetrically into an equilateral triangle [469–472]. To satisfy the equivalence condition for each neighboring pair interaction, each such emitter must also be rotated through $2\pi/3$, clockwise or counterclockwise, relative to its neighbor. Because the orientation of each emitter determines the angular displacement of its emitting dipole moment, the projection of the three dipoles onto the plane in which the array is placed is similar to the projection of a three-blade propeller. Using an array of molecular chromophores with such a triangular configuration, it is possible to design the necessary phase shifts for each of the emitters such that they correlate with the positions. Because each electric dipole is oriented at an angle of $\pm 2\pi/3$ with respect to two neighboring dipoles, the electric fields from each emitter add the phase factors $\{0, 2, 4\}\pi/3$ corresponding to the OV phase with the TC equal to 1 [467]. In the general case, the maximum TC ℓ is determined by the number of emitters N as $|\ell| \leqslant [(N-1)/2]$, where $[\ldots]$ is the integer part of a number. Although this approach has not yet been realized experimentally, the physical principles underlying it open up prospects for developing a vortex nanolaser based on the decay of nanosize excitons, to generate coherent radiation with a predetermined helical wavefront [470].

10. Interaction of intense vortex beams with nanosize structures and materials

At present, vortex laser beams have found wide application in various fields of modern photonics related to optical data transmission systems, methods of optical manipulation of microobjects, and superresolution optical microscopy. The interested reader can find a detailed description of these applications of vortex beams in a series of reviews [213, 473, 474]. Toward the end of this review, we focus on one promising area, which, however, has been discussed very

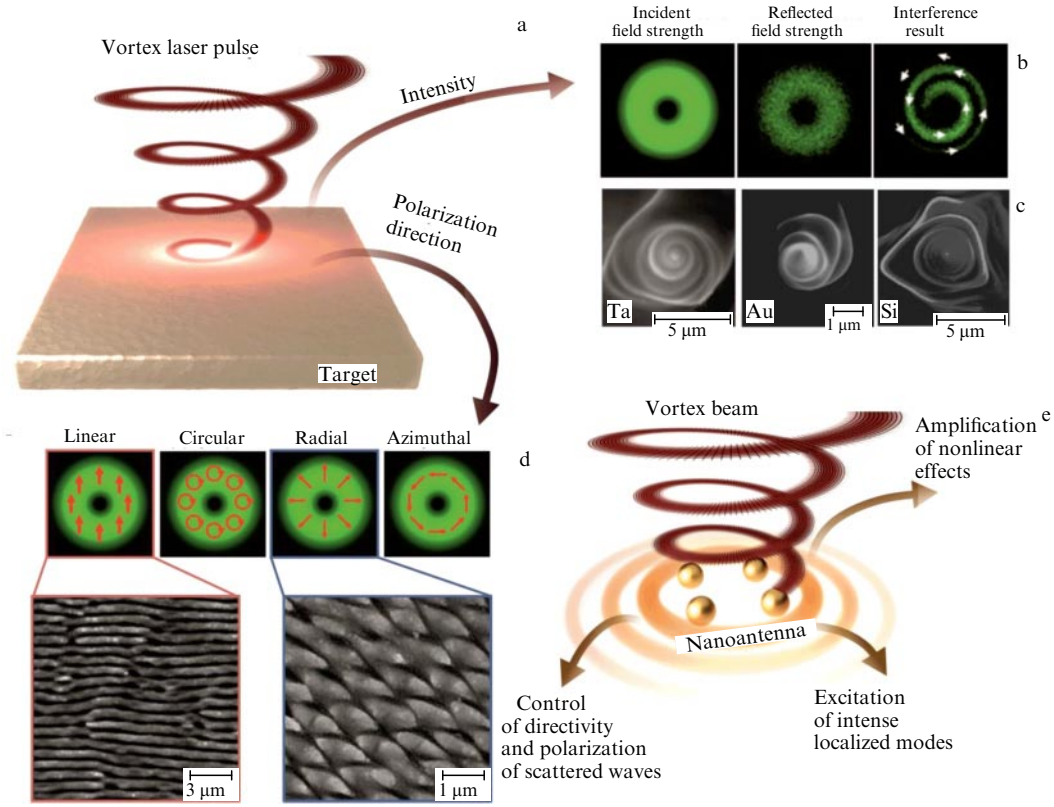

Figure 12. (Color online.) (a) Schematic illustration of the interaction of a sharply focused vortex laser pulse with a target surface. (b) Calculated distributions of the intensity of incident and reflected vortex beams from the surface and the result of their interference. (c) Series of SEM images of chiral microrelief formed on the surface of tantalum, gold, and silicon targets. (d) Polarization states that can be realized in a vortex laser beam (direction of the polarization vector is shown by red arrow) and SEM images of the surface of a nickel target textured by a laser beam with linear and radial polarizations. (e) Schematic representation of nanoantenna excitation by a vortex laser beam. (Figures b, c, and d are from [475, 477–479], and [492].)

little in previous reviews: the study of the interaction of intense singular beams with nanosize structures and various materials in application to problems in nanophotonics and laser nanotexturing of materials using short and ultrashort pulses.

First and foremost, the use of OVs opens up prospects for fundamental and applied studies of the interaction of high-power laser pulses of complex intensity and polarization profiles with various materials (Fig. 12a). In the last decade, the use of focused pulsed laser radiation to modify the surface of various targets has rapidly evolved from a laboratory method into an efficient and economically viable technology that, in terms of a number of characteristics, can compete with lithographic nanofabrication technologies in the near future. The multifaceted development of this method, among other things, was inseparably related to both the improvement and cost reduction of pulsed laser sources, not to mention a deep understanding of the complex processes underlying the formation of various types of functional micro- and nanostructures on the surface of irradiated targets under the action of laser radiation and the emergence of modern computational methods for modeling such ultrafast processes. At the same time, progress in OV generation methods has led to the appearance of commercial optical elements with a sufficiently high damage threshold to laser radiation (for example, S-wave plates), which made it possible to easily introduce singular beams into studies of the interaction of pulsed laser radiation with matter.

One of the clearest demonstrations of the promise of using OVs in laser nanostructuring is the possibility of forming chiral microstructures on the surface of various materials during their ablation by single nanosecond vortex laser pulses (Figs 12a–c). The effect has been demonstrated for various materials, including heavy and noble metals [475–478], semiconductors [326, 479–481], and polymers [482–484]. SEM images of chiral nanostructures formed under irradiation of tantalum, gold, and silicon targets are shown in Figs 12c. Because the direction of twist of the produced nanostructures typically coincides with the direction of rotation of the wave front of the OV material incident on the surface, it was hypothesized that the cause of the chiral morphology is the transfer of angular momentum from pulsed laser radiation to the target material. According to the authors, the impact of a laser pulse on the target surface leads to the melting of a local near-surface region, while the total angular momentum of the OV, determined by both circular polarization and wave front rotation, gives rise to the motion of molten material in the azimuthal direction, which makes the materials formed during microstructure recrystallization chiral. Moreover, the absence of this phenomenon when using pulses of shorter (femtosecond) duration to irradiate the surface does not contradict the above hypothesis, because the effects of light pressure are proportional to the laser exposure time.

An alternative explanation for the formation of a chiral nanorelief was proposed in [477]. The authors showed that, when a sharply focused vortex laser beam is incident on the target surface, a helical intensity distribution is formed as a result of interference between incident and reflected waves (Fig. 12b). Such a characteristic intensity distribution causes

the formation of corresponding temperature and surface tension distribution gradients, which leads to the azimuthal direction of motion of the substance melted under the action of the laser pulse and the formation of chiral nanostructures during recrystallization. Importantly, a helical intensity distribution can form only when the wave reflected from the target surface has a spherical wave front, and this becomes possible only when the vortex beam is not reflected from a smooth surface but from one with micro- and nano-rough morphology, which can be formed during the melting of the target surface under the action of laser radiation. Most of the metallic and semiconductor materials used in the context of these studies had typical electron-photon relaxation times (solid-to-liquid phase transition) of the order of several picoseconds, which justifies the absence of chiral morphology in nanostructures formed by irradiating a target with ultrashort femtosecond laser pulses. Later, this hypothesis was confirmed in experiments on single-pulse ablation of metal targets by linearly polarized nanosecond laser pulses with a helical intensity distribution profile and a flat wave front (zero total angular momentum) [477]. It is noteworthy that a similar explanation, based on the formation of a complex helical intensity distribution, was previously proposed to describe the effect of the formation of a chiral microrelief in azopolymers [482].

Currently, there are no theoretical studies in the literature aimed at a detailed description of the interaction of intense vortex laser pulses and matter. This is largely due to the complexity of constructing a rigorous theoretical model for the entire chain of laser-induced processes when the processes of photoexcitation of a material occurring in a time interval equal to the pulse duration are not separated in time from subsequent phase transitions, as is the case when using laser nanosecond pulses. At the same time, experimental demonstrations indicate that the use of laser beams with complex intensity and phase distribution profiles is a promising research direction, which allows significantly expanding the functionality of the methods of laser micro- and nanoprocessing of materials and extending the range of nanostructures obtained by these methods. An example of such a demonstration is the laser recording of three-dimensional chiral micropillars made of a photopolymerizable material using a three-dimensional helical intensity distribution obtained by combining two laser beams: an OV and a conventional Gaussian beam with a spherical wavefront [487–489].

The polarization distribution in a focal laser spot is known to have a significant effect on the micro- and nanomorphology of the target surface obtained by its multipulse irradiation with short and ultrashort laser pulses. This phenomenon is associated with ultrafast modulation (within the pulse duration times) of the intensity distribution profile in the laser spot due to the interference of the incident, reflected, and surface electromagnetic waves. Such intensity modulations lead to the formation of a characteristic self-organized or quasiperiodic morphology of the target surface (so-called laser-induced periodic surface structures, LIPSSs [490]) during its multipulse laser ablation by a scanning laser beam. The ability to control and switch polarization states in a vortex laser beam opens up broad prospects for the formation of unique LIPSS morphologies by multipulse ablation (Fig. 12d) [491]. For example, Skoulas et al. used femtosecond OV laser beams to treat nickel samples and create complex hierarchical surface morphologies that mimic shark skin and lotus leaf [491, 493]. The unique morphology of such nanotextured surfaces is shown in SEM images in Fig. 12d. Several theoretical studies have predicted the possibility of using pulsed OV laser beams to form topological defects of a certain type in chiral magnetic materials [494, 495]. In [494], it was proposed to use an OV beam for uneven heating of the irradiated surface of a chiral magnetic material and the formation of annular magnetic defects (skyrmions). To the best of our knowledge, no experimental demonstration of this effect has yet been reported.

The possibility of controlling the amplitude, phase, and polarization profiles of optical fibers opens up prospects for their use in the vibrant field of photonics of nanosize optical resonant structures [496, 501]. Unlike ordinary laser beams, OV beams can interact in a special way with optical resonant nanostructures by exciting certain resonant ('dark') modes in them (Fig. 12e), which cannot be excited using ordinary laser beams with a plane wavefront [500]. In this case, it is obvious that the characteristics of the OV beam used must be consistent with the geometry of the irradiated nanostructures in order to achieve the most efficient optical response. For example, control of the intensity and direction of scattering of a plasmonic nanoantenna made of two parallel nanorods was demonstrated when the center (phase singularity point) of the illuminating OV was displaced relative to the geometrical center of the nanoantenna [503]. In addition, the use of a radially polarized OV allowed exciting an anapole mode in a spherical silicon nanoantenna, which made it possible to completely suppress scattering into free space [504]. The possibility of observing the effect of circular dichroism during the passage of OV beams through a round nanosize aperture without any pronounced dichroic properties has also been demonstrated [501]. The effect arises because OV beams with opposite SAM signs are not mirror reflections of each other and interact in different ways, even with a geometrically symmetric nanoantenna. This ability of optical nanostructures to react resonantly to the chirality of optical radiation opens prospects for the development of microscale analyzers and built-in routers of optical beams for new-generation IOCs [500, 502, 503]. In particular, single nanosize holes and nanoantennas located along an annular trajectory have already demonstrated their efficiency as OAM analyzers for an optical beam incident on them. Finally, plasmonic and dielectric nanostructures, due to their ability to localize and amplify electromagnetic fields on nanoscales, allow achieving a significant enhancement of nonlinear effects (for example, the generation of higher-order harmonics or Kerr nonlinearity), which opens the door to the practical implementation of ultrafast optical switches and ultrasensitive sensor elements [504–506]. High-Q modes excited by OV beams in nanoantennas are typically characterized by high amplification factors for the amplitude of local electromagnetic fields, leading to a scalable amplification of nonlinear effects. For example, an increase in the intensity of third-harmonic generation was demonstrated when a single silicon nanoantenna was pumped by an OV beam, and the control of the polarization characteristics of the pump radiation also allows controlling the radiation polarization structure at the third-harmonic frequency [507]. A similar effect was recently demonstrated for an oligomer of silicon nanoparticles [508].

11. Conclusion

The demonstration of the presence of OAM in OV beams in the 1990s gave a powerful impetus to the development of new

efficient methods for their formation. The ability to control the motion of matter on nano- and microscales contributed to the development of the field of light robotics and micromechanics. Proof of the orthogonality of the states of OV beams with different OAM values contributed another degree of freedom to the implementation of optical communication systems based on mode multiplexing of data and opened the way to the implementation of data transmission channels with rates of several hundred Tbit s^{-1}. The use of OV beams in problems of classical and quantum optics, as well as in imaging, has already been covered in several reviews [216, 477, 478]. In recent years, OV beams have allowed demonstrating new effects in the field of laser processing of materials and in the field of manipulation of linear and nonlinear optical responses of resonant structures and optical antennas during their excitation. Hence, OVs and related phase singularities play an important role in modern science.

We emphasize that each of the specified sets of applications requires the use of a method to form optical beams with certain characteristics. For example, in forming unique chiral nano- and microreliefs on the surfaces of various materials, pulsed laser beams with sufficiently high energies must be used, which imposes certain requirements for the values of damage thresholds for the elements forming the OV beams. In this case, various types of diffractive optical elements fabricated on glass and quartz substrates, as well as nanostructured S-wave plates capable of withstanding huge power densities of laser radiation incident on them, up to 1 TW cm^{-2}, become ideal candidates. In applications that require constant reconfiguration of the profiles of shaped laser beams with OAM, such as light robotics and micromechanics, the key role is already played by the ability to quickly reconfigure the element profiles, which can easily be achieved using computer-calculated holograms realized with digital micromirror devices, as well as using the dynamical LC SLMs discussed in this review. LC technology allows realizing not only various holograms but also unique q-plates that ensure a switchable spin-orbit transformation with a switching time reaching 75 μs. And, of course, it is worth once again mentioning the trend toward miniaturization established in modern science and technology, which led to the development of vortex microelements and microlasers, without which it would be difficult to imagine the field of integrated optics and nanophotonics. Such elements fit within areas of several units or several ten square micrometers and allow not only forming OV beams but also tuning their TCs and the generated radiation wavelength. However, we must not forget a number of fairly simple methods for the formation of OV beams using various fork-shaped gratings and SFZPs: despite their apparent simplicity and the limitations of these approaches, they are an excellent demonstration for a first acquaintance with the field of singular optics and allow collecting basic knowledge of phase singularities and their formation and analysis. In addition, due to the possibility of relatively simple technological implementation, these methods allow focusing on the search for new effects that arise when using OV beams. This is confirmed, for example, by studies in which these elements were used to demonstrate the formation of a reverse energy flux, as well as stable 'rainbow' OV beams in white light.

This review is a guide to the world of OV beam formation methods and their topical applications, both for researchers with extensive experience in the field of structured laser beam formation and for those who are just beginning to grasp the basics of singular optics. Summary data for each of the considered formation methods must be helpful in making the right choice depending on the problem under consideration and in finding the most effective and appropriate solution. The development of new methods for the formation of OV beams does not stop at the present time, which gives confidence in the further successful development of studies of OAM light fields.

References

1. Nye J F, Berry M V *Proc. R. Soc. Lond. A* **336** 165 (1974)
2. Allen L et al. *Phys. Rev. A* **45** 8185 (1992)
3. Coullet P, Gil L, Rocca F *Opt. Commun.* **73** 403 (1989)
4. Soskin M S, Vasnetsov M V *Prog. Opt.* **42** 219 (2001)
5. Dennis M R, O'Holleran K, Padgett M J *Prog. Opt.* **53** 293 (2009)
6. Soskin M et al. *J. Opt.* **19** 010401 (2017)
7. Yao A M, Padgett M J *Adv. Opt. Photon.* **3** 161 (2011)
8. Rubinsztein-Dunlop H et al. *J. Opt.* **19** 013001 (2017)
9. Piccirillo B et al. *Riv. Nuovo Cimento* **36** 501 (2013)
10. Mehmood M Q et al. *J. Mol. Eng. Mater.* **2** 1440013 (2014)
11. Hernandez-Garcia C et al. *Photonics* **4** 28 (2017)
12. Wang X et al. *Nanophotonics* **7** 1533 (2018)
13. Zhang K et al. *Appl. Sci.* **10** 1015 (2019)
14. Shen Y et al. *Light Sci. Appl.* **8** 90 (2019)
15. Voitsekhovich V V, Kouznetsov D, Morozov D K *Appl. Opt.* **37** 4525 (1998)
16. Berry M V, Dennis M R *Proc. R. Soc. Lond. A* **456** 2059 (2000)
17. Mondragon R J, Berry M V *Proc. R. Soc. Lond. A* **424** 263 (1989)
18. Freund I *J. Opt. Soc. Am. A* **11** 1644 (1994)
19. Dennis M R *J. Opt. A* **6** S202 (2004)
20. Baranova N B et al. *JETP Lett.* **33** 195 (1981); *Pis'ma Zh. Eksp. Teor. Fiz.* **33** 206 (1981)
21. Baranova N B et al. *Sov. Phys. JETP* **56** 983 (1982); *Zh. Eksp. Teor. Fiz.* **83** 1702 (1982)
22. Baranova N B et al. *J. Opt. Soc. Am. A* **73** 525 (1983)
23. Wang W et al. *Phys. Rev. Lett.* **94** 103902 (2005)
24. Roux F S *Proc. SPIE* **9066** 906604 (2013)
25. Roux F S *J. Opt.* **15** 125722 (2013)
26. Roux F S *J. Opt.* **17** 045610 (2015)
27. Roux F S *J. Opt.* **18** 054005 (2016)
28. Freund I, Shvartsman N, Freilikher V *Opt. Commun.* **101** 247 (1993)
29. Soskin M S, Gorshkov V N, Vasnetsov M V *Phys. Rev. A* **56** 4064 (1997)
30. Berry M *J. Phys. A* **11** 27 (1978)
31. Freund I, Wilkinson M *J. Opt. Soc. Am. A* **15** 2892 (1998)
32. Dennis M R *J. Phys. A* **36** 6611 (2003)
33. Goodman J W *Speckle Phenomena in Optics*: *Theory and Applications* (Englewood, CO: Roberts and Co., 2007)
34. Sendra G H et al. *J. Opt. Soc. Am. A* **26** 2634 (2009)
35. Kirkpatrick S J et al. *J. Biomed. Opt.* **17** 050504 (2012)
36. Li X et al. *Opt. Commun.* **287** 6 (2013)
37. Li X et al. *Appl. Phys. B* **116** 901 (2014)
38. Majumdar A, Kirkpatrick S J *J. Biomed. Photon. Eng.* **4** 020301 (2018)
39. Vaughan J M, Willetts D V *Opt. Commun.* **30** 263 (1979)
40. Vaughan J M, Willetts D V *J. Opt. Soc. Am.* **73** 1018 (1983)
41. Tamm C *Phys. Rev. A* **38** 5960 (1988)
42. Harris M, Hill C A, Vaughan J M *Opt. Commun.* **106** 161 (1994)
43. Tamm C, Weiss C O *J. Opt. Soc Am. B* **7** 1034 (1990)
44. Abramochkin E, Volostnikov V *Opt. Commun.* **83** 123 (1991)
45. Oron R et al. *Appl. Phys. Lett.* **77** 3322 (2000)
46. Chen Y F, Lan, Y P, Wang S C *Appl. Phys. B* **72** 167 (2001)
47. Chen Y F, Lan Y P *Phys. Rev. A* **63** 063807 (2001)
48. Mose T et al. *Laser Phys. Lett.* **1** 234 (2004)
49. Bisson J F et al. *Opt. Rev.* **11** 353 (2004)
50. Bisson J F, Senatsky Y, Ueda K I *Laser Phys. Lett.* **2** 327 (2005)
51. Wang S et al. *Appl. Phys. Lett.* **112** 201110 (2018)
52. Huang X et al. *IEEE J. Sel. Top. Quantum Electron.* **24** 1601606 (2018)
53. Ma Y et al. *Opt. Express* **27** 18190 (2019)
54. Lin G et al. *Opt. Lett.* **43** 4164 (2018)

55. Kawauchi H et al. *Opt. Lett.* **33** 399 (2008)
56. Kim J W *J. Korean Phys. Soc.* **61** 739 (2012)
57. Kim J W et al. *Opt. Express* **19** 14526 (2011)
58. Machavariani G et al. *Appl. Opt.* **46** 3304 (2007)
59. Kozawa Y, Sato S *Opt. Lett.* **30** 3063 (2005)
60. Kim D J, Kim J W, Clarkson W A *Appl. Phys. B* **117** 459 (2014)
61. Kim D J, Kim J W *Opt. Lett.* **40** 399 (2015)
62. Zhang Q et al. *Chin. Opt. Lett.* **17** 051402 (2019)
63. Kim T H et al. *J. Korean Phys. Soc.* **75** 557 (2019)
64. Liu Q et al. *Laser Phys. Lett.* **15** 045002 (2018)
65. Ding M et al. *Opt. Lett.* **44** 4973 (2019)
66. Zheng S et al. *Photon. Res.* **8** 1375 (2020)
67. Caley A J et al. *Opt. Express* **15** 10699 (2007)
68. Zhang Z et al. *IEEE Photon. Technol. Lett.* **31** 1221 (2019)
69. Ito A, Kozawa Y, Sato S *J. Opt. Soc. Am. A* **27** 2072 (2010)
70. Kano K, Kozawa Y, Sato S *Int. J. Opt.* **2012** 359141 (2012)
71. Uesugi Y, Kozawa Y, Sato S *Opt. Lett.* **45** 2115 (2020)
72. Okida M et al. *Opt. Express* **15** 7616 (2007)
73. Chen Y et al. *Opt. Lett.* **45** 722 (2020)
74. Li N et al. *Photon. Res.* **7** 1209 (2019)
75. Kerridge-Johns W, Damzen M J *Opt. Express* **26** 32839 (2018)
76. Smith A V, Armstrong D J *Opt. Express* **11** 868 (2003)
77. Han D S, Kang M S *Photon. Res.* **7** 754 (2019)
78. Lee A J, Omatsu T, in *Vortex Dynamics and Optical Vortices* (Croatia: InTechOpen, 2017) Ch. 2
79. Lu J et al. *Laser Phys. Lett.* **14** 085807 (2017)
80. Zhoi N, Liu J, Wang J *Sci. Rep.* **8** 11394 (2018)
81. Forbes A *Laser Photon. Rev.* **13** 1900140 (2019)
82. Koyama M et al. *Opt. Express* **19** 994 (2011)
83. Koyama M et al. *Opt. Express* **19** 14420 (2011)
84. Aahdi A, Samanta G K *J. Opt.* **20** 01LT01 (2018)
85. Omatsu T, Miyamoto K, Lee A J *J. Opt.* **19** 123002 (2017)
86. Rego L et al. *Vortex Dynamics and Optical Vortices* (Croatia: InTechOpen, 2017) Ch. 9
87. Liu Q et al. *Opt. Mater.* **71** 31 (2017)
88. Sharma V, Aadhi A, Samanta G K *Opt. Express* **27** 18123 (2019)
89. Xu Z et al. *J. Opt.* **21** 025802 (2019)
90. Zheng J et al. *Photon. Res.* **6** 396 (2018)
91. Niu S et al. *Laser Phys. Lett.* **17** 045402 (2020)
92. Araki S et al. *Appl. Opt.* **57** 620 (2018)
93. Chen Y F et al. *Photon. Res.* **5** 561 (2017)
94. Kim J W, Clarkson W A *Opt. Commun.* **296** 109 (2013)
95. Chard S P, Shardlow P C, Damzen M J *Appl. Phys. B* **97** 275 (2009)
96. Lee A J, Omatsu T, Pask H M *Opt. Express* **21** 12401 (2013)
97. Zhang Z et al. *Laser Phys.* **30** 055102 (2020)
98. Wang S et al. *OSA Continuum* **2** 523 (2019)
99. Chen R S et al. *Appl. Phys. Lett.* **112** 261103 (2018)
100. Bazhenov V Yu, Vasnetsov M V, Soskin M S *JETP Lett.* **52** 429 (1990); *Pis'ma Zh. Eksp. Teor. Fiz.* **52** 1037 (1990)
101. Heckenberg N R et al. *Opt. Quantum Electron.* **24** S951 (1992)
102. Bazhenov V Y, Soskin M S, Vasnetsov V M *J. Mod. Opt.* **39** 985 (1992)
103. Basistiy I V, Soskin M S, Vasnetsov V M *Opt. Commun.* **119** 604 (1995)
104. Sacks Z S, Rozas D, Swartzlander Jr. G A *J. Opt. Soc. Am. B* **15** 2226 (2015)
105. Pas'ko V A et al. *Proc. SPIE* **5477** 83 (2004)
106. Basistiy I V et al. *J. Opt. A* **6** S166 (2004)
107. Janicijevic L, Topuzoski S *J. Opt. Soc. Am. A* **25** 2659 (2008)
108. Collier R J, Burckhardt C B, Lin L H *Optical Holography* (New York: Academic Press, 1971)
109. Song L, Lessard R A, Galarneau P *J. Mod. Opt.* **37** 1319 (1990)
110. Degtyarev S A et al. *J. Phys. Conf. Ser.* **735** 012023 (2016)
111. Khonina S N, Ustinov A V *Appl. Opt.* **58** 8227 (2019)
112. Padgett M et al. *J. Mod. Opt.* **49** 777 (2002)
113. Sola I J et al. *Appl. Phys. B* **91** 115 (2008)
114. Atencia J et al. *Opt. Express* **21** 21056 (2013)
115. Collados M-V et al. *Vortex Dynamics and Optical Vortices* (Croatia: InTechOpen, 2017) Ch. 8
116. Zhao J et al. *Proc. SPIE* **11427** 114271M (2020)
117. Roso L et al. *Appl. Phys. A* **92** 865 (2008)
118. Kotlyar V V, Kovalev A A, Porfirev A P *Appl. Opt.* **56** 4095 (2017)
119. Janicijevic L, Topuzoski S *Proc. Sixth Intern. Conf. Balkan Physical Union* **899** 333 (2007)
120. Moreno I et al. *Opt. Lett.* **34** 2927 (2009)
121. Bekshaev A Y, Orlinska O V *Opt. Commun.* **283** 1244 (2010)
122. Stoyanov L et al. *Opt. Commun.* **350** 301 (2015)
123. Bekshaev A Y, Karamoch A I *Opt. Commun.* **281** 3597 (2008)
124. Bekshaev A Y, Sviridova S V *Opt. Commun.* **283** 4866 (2010)
125. Khonina S N, Ustinov A V *Opt. Commun.* **426** 359 (2018)
126. Bekshaev A Y, Karamoch A I *Opt. Commun.* **281** 1366 (2008)
127. Bekshaev A, Orlinska O, Vasnetsov M *Opt. Commun.* **283** 2006 (2010)
128. Matta S et al. *J. Opt.* **20** 075604 (2018)
129. Xie Z et al. *Photon. Res.* **6** 743 (2018)
130. Miyamoto Y et al. *Proc. SPIE* **3740** 232 (1999)
131. Tudor R et al. *Romanian J. Inform. Sci. Technol.* **17** 389 (2014)
132. Liu Y J et al. *Appl. Phys. Lett.* **92** 101114 (2008)
133. Strohaber J, Scarborough T D, Uiterwaal C J *Appl. Opt.* **46** 8583 (2007)
134. Li S, Wang Z *Appl. Phys. Lett.* **103** 141110 (2013)
135. Ivanovskyy A A, Basistiy I V, Soskin M S *Semicond. Phys. Quantum Electron. Optoelectron.* **6** 249 (2003)
136. Carpentier A V et al. *Am. J. Phys.* **76** 916 (2008)
137. Kumar D, Das A, Boruah B R *Rev. Sci. Instrum.* **84** 026103 (2013)
138. Neo R et al. *Opt. Express* **22** 9920 (2014)
139. Huang D et al. *Am. J. Phys.* **80** 211 (2012)
140. Liu Y J et al. *Opt. Express* **15** 16645 (2007)
141. Infusino M et al. *Opt. Express* **20** 23138 (2012)
142. Wei B Y et al. *Adv. Mater.* **26** 1590 (2014)
143. Chen P et al. *Photon. Res.* **3** 133 (2015)
144. Ge S J et al. *Opt. Mater. Express* **4** 2535 (2014)
145. Heckenberg N R et al. *Opt. Lett.* **17** 221 (1992)
146. Soskin M S, Polyanskii P V, Arkhelyuk O O *New J. Phys.* **6** 196 (2004)
147. Iizuka K *Elements of Photonics* Vol. 1 (New York: John Wiley and Sons, 2002)
148. Kreis T *Handbook of Holographic Interferometry: Optical and Digital Methods* (New York: Wiley-VCH, 2005)
149. Londono N et al. *Appl. Opt.* **54** 796 (2015)
150. Bock M, Jahns J, Grunwald R *Opt. Lett.* **37** 3804 (2012)
151. Tamburini F et al. *Nat. Phys.* **7** 195 (2011)
152. Wojnowski D et al. *Opt. Lett.* **39** 119 (2014)
153. Ribic R P et al. *Phys. Rev. X* **7** 031036 (2017)
154. Benk M P et al. *J. Micro/Nanolith. MEMS MOEMS* **14** 013507 (2015)
155. Kozlova E S *Comput. Opt.* **42** 977 (2018)
156. Zheng C et al. *Appl. Opt.* **57** 3802 (2018)
157. Cheng S et al. *IEEE Photon. J.* **11** 4500111 (2019)
158. Gao N et al. *Appl. Phys. Lett.* **98** 151106 (2011)
159. Sabatyan A, Balanoji S T *J. Opt. Soc. Am. A* **33** 1793 (2016)
160. Yu J et al. *Appl. Opt.* **51** 6799 (2012)
161. Wei L et al. *J. Opt. Soc. Am. A* **30** 233 (2013)
162. Balcytis A et al. *Opt. Express* **24** 16988 (2016)
163. Balcytis A et al. *MATEC Web Conf.* **32** 03002 (2015)
164. Zhang Y, Xie C *Opt. Commun.* **311** 65 (2013)
165. Raghdoost J, Sabatyan A *J. Opt. Soc. Am. B* **34** 608 (2016)
166. Ji Z et al. *J. Opt. Soc. Am. A* **35** 726 (2018)
167. Zang H-P et al. *Chin. Phys. B* **28** 064201 (2019)
168. Yang J et al. *J. Opt. Soc. Am. A* **36** 893 (2019)
169. Zang H et al. *Appl. Opt.* **58** 8680 (2019)
170. Liang Y et al. *Opt. Lett.* **42** 2663 (2017)
171. Fernandez R et al. *Polymers* **11** 1920 (2019)
172. Lu Y-M et al. *IEEE Photon. Technol. Lett.* **31** 979 (2019)
173. Gao S et al. *Opt. Lett.* **45** 2684 (2020)
174. Anand S *Opt. Commun.* **282** 1335 (2009)
175. Gauthier D et al. *Opt. Lett.* **44** 546 (2019)
176. Liang Y et al. *Opt. Lett.* **44** 935 (2019)
177. Khonina S N et al. *Opt. Commun.* **91** 158 (1992)
178. Kotlyar V V et al. *J. Opt. Soc. Am. A* **24** 1955 (2007)
179. Kotlyar V V et al. *J. Opt. Technol.* **74** 686 (2007)
180. Curtis J E, Koss B A, Grier D G *Opt. Commun.* **207** 169 (2002)
181. Crabtree K, Davis J A, Moreno I *Appl. Opt.* **43** 1360 (2004)
182. Vyas S, Singh R K, Senthilkumaran P *Opt. Laser Technol.* **42** 878 (2010)

183. Vyas S et al. *Int. J. Opt.* **2012** 249695 (2012)
184. Tao S H et al. *Appl. Phys. Lett.* **89** 031105 (2006)
185. Furlan W D et al. *Opt. Express* **17** 21891 (2009)
186. Calatayud A et al. *Appl. Phys. B* **106** 915 (2012)
187. Mitry M et al. *Appl. Opt.* **51** 4103 (2012)
188. Wu D et al. *Opt. Lett.* **33** 2913 (2008)
189. Arlt J et al. *J. Mod. Opt.* **45** 1231 (1998)
190. Mirhosseini M et al. *Opt. Express* **21** 30204 (2013)
191. Ruffato G, Massari M, Romanato F *Opt. Lett.* **39** 5094 (2014)
192. Huang S, He C, Wang T *J. Opt.* **16** 035402 (2014)
193. Watanabe T et al. *Opt. Eng.* **43** 1136 (2004)
194. Vijayakumar A, Bhattacharya S *Opt. Eng.* **54** 111310 (2015)
195. Chavez-Cerda S et al. *J. Opt. B* **4** S52 (2002)
196. Kotlyar V V, Kovalev A A, Volynov M V *Comput. Opt.* **40** 765 (2016)
197. Kotlyar V V, Kovalev A A, Soifer V A *Comput. Opt.* **39** 299 (2015)
198. Guo C S et al. *J. Opt. Soc. Am. A* **22** 385 (2005)
199. Kovalev A A, Kotlyar V V *J. Opt. Soc. Am. A* **36** 142 (2019)
200. Kotlyar V V, Kovalev A A, Porfirev A P *Comput. Opt.* **41** 330 (2017)
201. Kotlyar V V et al. *Opt. Lett.* **32** 742 (2007)
202. Kotlyar V V et al. *Appl. Opt.* **47** 6124 (2008)
203. Chen J, Wang G, Xu Q *Opt. Eng.* **50** 024201 (2011)
204. Balanoi S M T, Sabatyan A *J. Opt. Soc. Am. B* **35** 2667 (2018)
205. Ostrovsky A S, Rickenstor-Parrao C, Arrizon V *Opt. Lett.* **38** 534 (2013)
206. Kotlyar V V, Kovalev A A, Porfirev A P *J. Opt. Soc. Am. A* **33** 2376 (2016)
207. Porfirev A, Kuchmizhak A *Appl. Phys. Lett.* **113** 171105 (2018)
208. Kotlyar V V, Kovalev A A, Porfirev A P *Optik* **156** 49 (2018)
209. Kotlyar V V, Kovalev A A, Porfirev A P *Comput. Opt.* **40** 312 (2016)
210. Kovalev A A, Kotlyar V V, Porfirev A P *Phys. Rev. A* **91** 053840 (2015)
211. Kovalev A A, Kotlyar V V, Porfirev A P *Phys. Rev. A* **93** 063858 (2016)
212. Kotlyar V V, Kovalev A A, Porfirev A P *Phys. Rev. A* **95** 053805 (2017)
213. Kotlyar V V, Kovalev A A *Accelerating and Vortex Laser Beams* (Boca Raton, FL: CRC Press, 2019)
214. Aksenov V P et al. *Opt. Spectrosc.* **124** 273 (2018); *Opt. Spektrosk.* **124** 275 (2018)
215. Kotlyar V V, Kovalev A A, Porfirev A P *Vortex Laser Beams* (Boca Raton, FL: CRC Press, 2018)
216. Ustinov A V *Comput. Opt.* **41** 617 (2017)
217. Skidanov R V, Ganchevskaya S V *Comput. Opt.* **39** 674 (2015)
218. Khonina S N et al. *J. Mod. Opt.* **39** 1147 (1992)
219. Higgins T V *Laser Focus World* **28** 18 (1992)
220. Bryngdahl O *J. Opt. Soc. Am.* **63** 1098 (1973)
221. Beijersbergen M W et al. *Opt. Commun.* **112** 321 (1994)
222. Moh K J et al. *Appl. Opt.* **45** 1153 (2005)
223. Baghdady J et al. *Opt. Express* **24** 9794 (2016)
224. Kotlyar V V et al. *J. Opt.* **15** 025712 (2013)
225. Kotlyar V V et al. *Opt. Lett.* **31** 1597 (2006)
226. Kotlyar V V et al. *J. Opt. Soc. Am. A* **22** 849 (2005)
227. Kotlyar V V et al. *Appl. Opt.* **45** 2656 (2006)
228. Miler M et al. *Proc. SPIE* **3573** 461 (1998)
229. Oemrawsingh S R et al. *Appl. Opt.* **43** 688 (2004)
230. Massari M et al. *Appl. Opt.* **54** 4077 (2015)
231. Prasciolu M et al. *Microelectron Eng.* **86** 1103 (2009)
232. Massari M et al. *Microelectron. Eng.* **88** 2675 (2011)
233. Paul S et al. *Opt. Lett.* **41** 3249 (2016)
234. Brasselet E et al. *Appl. Phys. Lett.* **97** 211108 (2010)
235. Zukauskas A, Malinauskas M, Brasselet E *Appl. Phys. Lett.* **103** 181122 (2013)
236. Lyubopytov V S et al. *Opt. Express* **25** 9634 (2017)
237. Wei H, Amrithanath A K, Krishnaswamy S *IEEE Photon. Technol. Lett.* **31** 599 (2019)
238. Chen J et al. *Chin. Phys. Lett.* **26** 014202 (2009)
239. Li H et al. *Optica* **2** 547 (2015)
240. Rodrigues Ribeiro R S et al. *Proc. SPIE* **9764** 97640Q (2016)
241. Miyamoto K et al. *Appl. Phys. Lett.* **104** 261104 (2014)
242. Miyamoto K et al. *Sci. Rep.* **6** 38880 (2016)
243. Sun J et al. *Sci. Rep.* **4** 4093 (2014)
244. Xin J et al. *Opt. Lett.* **39** 1984 (2014)
245. Campbell G et al. *Appl. Opt.* **51** 873 (2012)
246. Shen Y et al. *J. Opt.* **15** 044005 (2013)
247. Sueda K et al. *Opt. Express* **12** 3548 (2004)
248. Kotlyar V V, Kovalev A A *Opt. Lett.* **33** 189 (2008)
249. Rueda E et al. *Opt. Lett.* **38** 3941 (2013)
250. Berry M V *J. Opt. A* **6** 259 (2004)
251. Lee W M, Yuan X C, Dholakia K *Opt. Commun.* **239** 129 (2004)
252. Rotschild C et al. *Appl. Opt.* **43** 2397 (2004)
253. Leach J, Yao E, Padgett M J *New. J. Phys.* **6** 71 (2004)
254. Zhang N et al. *Appl. Opt.* **49** 2456 (2010)
255. Na Y, Ko D-K *Sci. Rep.* **11** 2678 (2021)
256. Khonina S N, Porfirev A P, Ustinov A V *J. Opt.* **17** 125607 (2015)
257. Moh X C et al. *Appl. Phys. Lett.* **88** 091103 (2006)
258. Swartzlander Jr. G A *Opt. Lett.* **31** 2042 (2006)
259. Xie Q, Zhao D *Opt. Commun.* **281** 7 (2008)
260. Yuan X C et al. *Opt. Express* **16** 13599 (2008)
261. Wang Q et al. *Opt. Express* **13** 10285 (2005)
262. Algorri J F et al. *IEEE Electron Device Lett.* **35** 856 (2014)
263. Bernet S, Ritsch-Marte M *Appl. Opt.* **47** 3722 (2008)
264. Harm W et al. *Opt. Express* **23** 413 (2015)
265. Khonina S N et al. *Opt. Express* **28** 18407 (2020)
266. Gai D P, Senthilkumaran P, Sirohi R S *Appl. Opt.* **47** 1378 (2008)
267. Gai D P *Appl. Opt.* **50** 1374 (2011)
268. Tyson R K, Scipioni M, Viegas J *Appl. Opt.* **47** 6300 (2008)
269. Ament C et al. *Appl. Opt.* **53** 3355 (2014)
270. Li H et al., in *Proc. of the Conf. on Lasers and Electro-Optics-2015, CLEO 2015*
271. Knoner G et al. *Opt. Express* **15** 5521 (2007)
272. Zhang L et al. *J. Opt. Soc. Am. A* **35** 1599 (2018)
273. Lin Y-Y et al. *J. Opt.* **20** 075203 (2018)
274. King T A et al. *Opt. Commun.* **187** 407 (2001)
275. Volyar A V, Fadeeva T A, Egorov Yu A *Tech. Phys. Lett.* **28** 958 (2002); *Pis'ma Zh. Eksp. Teor. Fiz.* **28** (22) 70 (2002)
276. Volyar A V, Fadeeva T A *Opt. Spectrosc.* **94** 235 (2003); *Opt. Spektrosk.* **94** 264 (2003)
277. Ciattoni A, Cincotti G, Palma C *J. Opt. Soc. Am. A* **20** 163 (2003)
278. Volyar A V, Fadeeva T A *Opt. Spectrosc.* **101** 450 (2006) *Opt. Spektrosk.* **101** 477 (2006); *Opt. Spektrosk.* **101** 477 (2006)
279. Brasselet E *Opt. Lett.* **34** 1021 (2009)
280. Khonina S N, Kharitonov S I *J. Mod. Opt.* **62** 125 (2014)
281. Fadeyeva T A, Volyar A V *J. Opt. Soc. Am. A* **27** 381 (2010)
282. Khonina S N, Morozov A A, Karpeev S V *Laser Phys.* **24** 056101 (2014)
283. Khonina S N et al. *Phys. Lett. A* **381** 2444 (2017)
284. Fadeyeva T et al. *J. Opt. Soc. Am. A* **25** 1634 (2008)
285. Fadeyeva T A, Rubass A F, Volyar A V *Phys. Rev. A* **79** 053815 (2009)
286. Fadeyeva T A et al. *Opt. Express* **18** 10848 (2010)
287. Fadeyeva T A et al. *J. Opt.* **15** 044020 (2013)
288. Shvedov V G et al. *Opt. Lett.* **35** 2660 (2010)
289. Berry M V, Klein S *Proc. Natl. Acad. Sci. USA* **93** 2614 (1996)
290. Berry M V *New J. Phys.* **4** 66 (2002)
291. Berry M V *New J. Phys.* **4** 74 (2002)
292. Egorov Y A, Fadeyeva T A, Volyar A V *J. Opt. A* **6** S217 (2004)
293. Volyar A V et al. *Tech. Phys. Lett.* **30** 701 (2004); *Pis'ma Zh. Eksp. Teor. Fiz.* **30** (16) 82 (2004)
294. Fallet C, Sirat G Y *Opt. Lett.* **41** 769 (2016)
295. Bomzon Z, Kleiner V, Hasman E *Opt. Lett.* **26** 1424 (2001)
296. Bomzon Z et al. *Opt. Lett.* **27** 1141 (2002)
297. Biener G et al. *Opt. Lett.* **27** 1875 (2002)
298. Levy U et al. *Opt. Lett.* **30** 2089 (2005)
299. Hasman E et al. *Appl. Phys. Lett.* **82** 328 (2003)
300. Niv A et al. *Opt. Commun.* **2515** 306 (2005)
301. Niv A et al. *Opt. Lett.* **30** 2933 (2005)
302. Niv A et al. *Opt. Express* **14** 4208 (2006)
303. Wang X et al. *Appl. Phys. Lett.* **110** 181101 (2017)
304. Hua J-G et al. *Appl. Surf. Sci.* **475** 660 (2019)
305. Marrucci L, Manzo C, Paparo D *Appl. Phys. Lett.* **88** 221102 (2006)
306. Marrucci L, Manzo C, Paparo D *Phys. Rev. Lett.* **96** 163905 (2006)
307. Marrucci L *Mol. Cryst. Liq. Cryst.* **488** 148 (2008)
308. Karimi E et al. *Opt. Lett.* **34** 1225 (2009)
309. Varghese S et al. *Appl. Phys. Lett.* **85** 230 (2004)
310. Chen J et al. *Appl. Phys. Lett.* **67** 1990 (1995)

311. Schadt M, Seiberle H, Schuster A *Nature* **381** 212 (1996)
312. Aizawa M et al. *J. Opt. Soc. Am. B* **36** D47 (2019)
313. Karimi E et al. *Appl. Phys. Lett.* **94** 231124 (2009)
314. Piccirillo B et al. *Appl. Phys. Lett.* **97** 241104 (2010)
315. Slussarenko S et al. *Opt. Express* **19** 4085 (2011)
316. Kravets N et al. *Appl. Phys. Lett.* **114** 061101 (2019)
317. Radhakrishna B, Kadiri G, Radhavan G *Sci. Rep.* **9** 11911 (2019)
318. Zheng S et al. *Opt. Express* **27** 16103 (2019)
319. Liu Y et al. *Opt. Express* **27** 36903 (2019)
320. Marrucci L *J. Nanophoton.* **7** 078598 (2013)
321. Cardano F et al. *Appl. Opt.* **51** C1 (2012)
322. Cardano F, Marrucci L *Nat. Photon.* **9** 776 (2015)
323. Yan L et al. *Optica* **2** 900 (2015)
324. Davis J A et al. *Appl. Opt.* **54** 9583 (2015)
325. Nivas J J et al. *Opt. Lett.* **40** 4611 (2015)
326. Rahimian M G et al. *APL Photon.* **2** 086104 (2017)
327. Naidoo D et al. *Nat. Photon.* **10** 327 (2016)
328. Rubano A et al. *J. Opt. Soc. Am. B* **36** D70 (2019)
329. Vergaga M, Iemmi C *Phys. Rev. A* **100** 053812 (2019)
330. Taylor R, Hnatovsky C, Simova E *Laser Photon. Rev.* **2** 26 (2008)
331. Sun H-B et al. *J. Phys. Chem. B* **104** 3450 (2000)
332. Davis K et al. *Opt. Lett.* **21** 1729 (1996)
333. Glezer E, Mazur E *Appl. Phys. Lett.* **71** 18 (1997)
334. Kazansky P et al. *Phys. Rev. Lett.* **82** 2199 (1999)
335. Shimotsuma Y et al. *Phys. Rev. Lett.* **91** 247405 (2003)
336. Bhardwaj V et al. *Phys. Rev. Lett.* **96** 057404 (2006)
337. Beresna B et al. *Appl. Phys. Lett.* **98** 201101 (2011)
338. Beresna B, Geceviius M, Kazansky P *Opt. Mater. Express* **1** 783 (2011)
339. Huang B et al. *Opt. Express* **25** 30 (2017)
340. Wortmann D et al. *Opt. Express* **16** 1517 (2008)
341. Shimotsuma Y et al. *Jpn. J. Appl. Phys.* **44** 4735 (2005)
342. Shimotsuma Y et al. *Mod. Phys. Lett. B* **19** 225 (2005)
343. Lancry M et al. *Opt. Mater. Express* **1** 711 (2011)
344. Richter S et al. *Opt. Mater. Express* **3** 1161 (2013)
345. Richter S et al. *Opt. Mater. Express* **5** 1834 (2015)
346. Zimmermann F et al. *Appl. Phys. Lett.* **104** 211107 (2014)
347. Fedotov S S et al. *Appl. Phys. Lett.* **108** 071905 (2016)
348. Drevinskas R, Kazansky P G *APL Photon.* **2** 066104 (2017)
349. Gecevicius M et al. *J. Opt. Soc. Am. B* **35** 190 (2018)
350. Hernandez-Garcia C et al. *Optica* **4** 520 (2017)
351. Gegevilius M et al. *Appl. Phys. Lett.* **104** 231110 (2014)
352. Brasselet E et al. *Phys. Rev. Lett.* **103** 103903 (2009)
353. Brasselet E, Loussert C *Opt. Lett.* **36** 719 (2011)
354. Brasselet E *Phys. Rev. Lett.* **108** 087801 (2012)
355. Loussert C, Delabre U, Brasselet E *Phys. Rev. Lett.* **111** 037802 (2013)
356. Barboza R et al. *Phys. Rev. Lett.* **111** 093902 (2013)
357. Brasselet E *Phys. Rev. Lett.* **121** 033901 (2018)
358. Kravets N, Brasselet E *J. Opt.* **22** 034001 (2020)
359. Barboza R et al. *Adv. Opt. Photon.* **7** 635683 (2015)
360. Oldenbourg R *Biophys. J.* **60** 629 (1991)
361. Beresna M et al. *Opt. Express* **19** 18989 (2011)
362. Daly M, Sergides M, Chormaic S *Laser Photon. Rev.* **9** 309 (2015)
363. Gao D et al. *Light Sci Appl.* **6** e17039 (2017)
364. Conteduca V et al. *Appl. Spectrosc.* **71** 367 (2017)
365. Raether H *Surface Plasmons* (Berlin: Springer, 1988)
366. Homola J, Yee S, Gauglitz G *Sensors Actuat. B* **54** 3 (1999)
367. Barnes W, Dereux A, Ebbesen T *Nature* **424** 824 (2003)
368. Kneipp K et al. *Phys. Rev. Lett.* **78** 1667 (1997)
369. Kazanskiy N L et al. *Comput. Opt.* **44** 295 (2020)
370. Gorodetski Y et al. *Phys. Rev. Lett.* **101** 043903 (2008)
371. Kim H et al. *Nano Lett.* **10** 529 (2010)
372. Zhou H et al. *IEEE Photon. J.* **7** 4801007 (2015)
373. Chen W et al. *Nano Lett.* **10** 2075 (2010)
374. Tsai W Y, Huang J S, Huang C B *Nano Lett.* **14** 547 (2014)
375. Ku C T, Lin H N, Huang C B *Appl. Phys. Lett.* **106** 053112 (2015)
376. Wang Y et al. *Sci. Rep.* **6** 36269 (2016)
377. Huang F et al. *Plasmonics* **12** 751 (2017)
378. Zhang Q et al. *J. Nanophoton.* **12** 1 (2018)
379. Gorodetski Y et al. *Phys. Rev. Lett.* **110** 203906 (2013)
380. Garoli D et al. *Sci. Rep.* **6** 29547 (2016)
381. Garoli D et al. *Nano Lett.* **16** 6636 (2016)
382. Maccaferri N et al. *Appl. Phys. Lett.* **111** 201104 (2017)
383. David A, Gjonaj B, Bartal G *Phys. Rev. B* **93** 121302 (2016)
384. Ku C D et al. *IEEE Photon. J.* **5** 4800409 (2013)
385. Ostrovsky E E et al. *Optica* **5** 283 (2018)
386. Khoo E H, Ahmed I, Li E P *Appl. Phys. Lett.* **102** 131104 (2013)
387. Spektor G et al. *Science* **355** 1187 (2017)
388. Aieta F et al. *Nano Lett.* **12** 4932 (2012)
389. Zheng G et al. *Nat. Nanotechnol.* **10** 308 (2015)
390. Huang L et al. *Nat. Commun.* **4** 2808 (2013)
391. Yu N et al. *Nano Lett.* **12** 6328 (2012)
392. Yu N et al. *Science* **334** 333 (2011)
393. Yu N, Capasso F *Nat. Mater.* **13** 139 (2014)
394. Meinzer N, Barnes W, Hooper I *Nat. Photon.* **8** 889 (2014)
395. Khorasaninejad M, Capasso F *Science* **358** eaam8100 (2017)
396. Genevet P et al. *Optica* **12** 139 (2017)
397. Ni X et al. *Science* **335** 427 (2011)
398. Genevet P et al. *Appl. Phys. Lett.* **100** 013101 (2012)
399. Karimi E et al. *Light Sci. Appl.* **3** E167 (2014)
400. Huang L et al. *Nano Lett.* **12** 5750 (2012)
401. Bouchard F et al. *Appl. Phys. Lett.* **105** 101905 (2014)
402. Liu L et al. *Adv. Mater.* **26** 5031 (2014)
403. Zeng J et al. *Nano Lett.* **16** 3101 (2016)
404. Chen S et al. *Laser Photon. Rev.* **10** 322 (2016)
405. Mehmood M et al. *Adv. Mater.* **28** 2533 (2016)
406. Sun J et al. *Nano Lett.* **14** 2726 (2014)
407. Guo Y et al. *ACS Photon.* **3** 2022 (2016)
408. Pors A et al. *Nano Lett.* **3** 829 (2013)
409. Hakobyan D et al. *Adv. Opt. Mater.* **4** 306 (2015)
410. Chen W et al. *Nano Lett.* **14** 225 (2014)
411. Lin D et al. *Science* **345** 298302 (2014)
412. Arbabi A et al. *Nat. Nanotechnol.* **10** 937943 (2015)
413. Shalaev M et al. *Nano Lett.* **15** 6261 (2015)
414. Glybovski S et al. *Phys. Rep.* **634** 1 (2016)
415. Decker M et al. *Adv. Opt. Mater.* **3** 813 (2015)
416. Pfeiffer C, Grbic A *Phys. Rev. Lett.* **110** 197401 (2013)
417. Dharmavarapu R et al. *Opt. Express* **28** 3505 (2020)
418. Devlin R et al. *Opt. Express* **25** 377 (2017)
419. Xie Y-Y et al. *Nat. Nanotechnol.* **15** 125 (2020)
420. Devlin R C et al. *Science* **358** 896 (2017)
421. Wang S et al. *J. Phys. D* **52** 324002 (2019)
422. Sroor H et al. *Nat. Photon.* **14** 498 (2020)
423. Nape I et al. *APL Photon.* **5** 070802 (2020)
424. Huang Y-W *Opt. Express* **27** 7469 (2019)
425. Zhou H et al. *Appl. Phys. B* **124** 42 (2019)
426. Seniutinas G et al. *Nanophotonics* **6** 923 (2017)
427. Wang X et al. *Phys. Rev. Appl.* **8** 044016 (2017)
428. Zhu X et al. *Nat. Nanotechnol.* **11** 325 (2016)
429. Zhu X et al. *Sci. Adv.* **3** e1602487 (2017)
430. Zograf G et al. *Nano Lett.* **17** 2945 (2017)
431. Ma R-M, Oulton R F *Nat. Nanotechnol.* **14** 12 (2019)
432. Jiang Y, Cao Y, Feng X *J. Phys. D* **53** 303002 (2020)
433. Chen Y et al. *Phys. Rev. Lett.* **127** 153601 (2020)
434. Liu J et al. *Light Sci. Appl.* **7** 17148 (2018)
435. Yu Y F et al. *Opt. Express* **18** 21651 (2010)
436. Doerr C R, Buhl L L *Opt. Lett.* **36** 1209 (2011)
437. Fontaine N K, Doerr C R, Buhl L, OSA Tech. Digest, Optical Society of America OTu1I.2 (2012)
438. Cai X et al. *Science* **338** 363 (2012)
439. Cai X L, Chen Y J, Yu S Y *Sci. China B* **56** 579 (2013)
440. Zhu J et al. *Opt. Lett.* **38** 1343 (2013)
441. Li H et al., in *Progress in Electromagnetic Research Symp.* (*PIERS*) (2016)
442. Cognee K G et al. *ACS Photon.* **7** 3049 (2020)
443. Li S et al. *Opt. Lett.* **43** 1319 (2018)
444. Xiao Q et al. *Opt. Express* **24** 3168 (2016)
445. Wang Y et al. *Sci. Rep.* **5** 10958 (2015)
446. Schulz S et al. *Opt. Express* **21** 16130 (2013)
447. Zhang D et al. *IEEE Photon. J.* **5** 2201206 (2013)
448. Mochizuki S et al. *Appl. Phys. Express* **7** 022502 (2014)
449. Guan B et al. *Opt. Express* **22** 145 (2014)
450. Zhang D et al. *IEEE Photon. J.* **6** 2200710 (2014)
451. Miao P et al. *Science* **353** 464 (2016)
452. Zhang J et al. *Nat. Commun.* **9** 2652 (2018)

453. Zhang Z et al. *Science* **368** 760 (2020)
454. Zhang Z et al. *Light Sci. Appl.* **9** 179 (2020)
455. Hayenga W E et al. *ACS Photon.* **6** 1895 (2019)
456. Zambon N C et al. *Nat. Photon.* **13** 283 (2019)
457. Mock A, Sounas D, Alu A *Phys. Rev. Lett.* **121** 103901 (2018)
458. Xie Z et al. *Light Sci. Appl.* **7** 18001 (2018)
459. Stellinga D et al. *ASC Nano* **12** 2389 (2018)
460. Qian H, Markman B D, Giebink N C *Appl. Phys. Rev.* **103** 161110 (2013)
461. Kuehne A C, Gather M C *Chem. Rev.* **116** 12823 (2016)
462. Sun W et al. *Nat. Commun.* **11** 4862 (2020)
463. Kodigala A et al. *Nature* **541** 196 (2017)
464. Huang C et al. *Science* **367** 1017 (2020)
465. Wang B et al. *Nat. Photon.* **14** 623 (2020)
466. Yin X, Peng C *Photon. Res.* **8** B25 (2020)
467. Williams W D et al. *Phys. Rev. Lett.* **111** 153603 (2013)
468. Andrews D L et al. *Proc. SPIE* **8813** 88130Y (2013)
469. Ford J S, Bradshaw D S, Andrew D L *J. Phys. Chem. C* **117** 12393 (2013)
470. Williams W D et al. *Phys. Rev. A* **89** 033837 (2014)
471. Williams W D, Bradshaw D S, Andrews D L *Proc. SPIE* **9126** 91260F (2014)
472. Coles M M et al. *Laser Photon. Rev.* **7** 1088 (2013)
473. Bliokh K et al. *Nat. Photon.* **9** 796 (2015)
474. Aiello A et al. *Nat. Photon.* **9** 789 (2015)
475. Toyoda K et al. *Nano Lett.* **12** 3645 (2012)
476. Toyoda K et al. *Phys. Rev. Lett.* **110** 143603 (2013)
477. Syubaev S et al. *Opt. Express* **25** 10214 (2017)
478. Syubaev S et al. *Appl. Surf. Sci.* **470** 526 (2019)
479. Takahashi F et al. *Sci. Rep.* **6** 21738 (2016)
480. Takahashi F et al. *Phys. Status Solidi A* **213** 1063 (2015)
481. Syubaev S et al. *Opt. Lett.* **45** 3050 (2020)
482. Ambrosio A et al. *Nat. Commun.* **3** 989 (2013)
483. Marrucci L, Ambrosio A, Maddalena P *Phys. Rev. Lett.* **110** 989 (2013)
484. Watabe M et al. *Sci. Rep.* **4** 4281 (2014)
485. Syubaev S et al. *Opt. Lett.* **42** 5022 (2017)
486. Hnatovsky C et al. *Opt. Lett.* **30** 1867 (2005)
487. Ni J et al. *Light Sci. Appl.* **6** e17011 (2017)
488. Ni J et al. *Adv. Func. Mater.* **27** 1701939 (2017)
489. Rektyt S et al. *Adv. Opt. Mater.* **4** 1209 (2016)
490. Buividas R, Mikutis M, Juodkazis S *Prog. Quantum Electron.* **38** 119 (2014)
491. Nivas J et al. *Sci. Rep.* **5** 17929 (2015)
492. Skoulas E et al. *Sci. Rep.* **7** 45114 (2017)
493. Wang L et al. *Light Sci. Appl.* **6** e17112 (2017)
494. Fujita H, Sato M *Phys. Rev. B* **95** 054421 (2017)
495. Fujita H, Sato M *Phys. Rev. B* **96** 060407(R) (2017)
496. Giannini V et al. *Chem. Rev.* **111** 3888 (2011)
497. Kuznetsov A et al. *Nat. Photon.* **354** aag2472 (2016)
498. Wei L et al. *Optica* **5** 4922 (2016)
499. Xi Z et al. *Phys. Rev. Lett.* **117** 113903 (2016)
500. Kerber R et al. *ACS Photon.* **4** 891 (2017)
501. Zambrana-Puyalto X, Vidal X, MolinaTerriza G *Nat. Commun.* **5** 4922 (2017)
502. Ren X et al. *Science* **4** 891 (2016)
503. Wei D et al. *ACS Photon.* **4** 996 (2017)
504. Kauranen M, Zayats A *Nat. Photon.* **6** 737 (2012)
505. Makarov S et al. *Laser Photon. Rev.* **11** 1700108 (2017)
506. Syubaev S A et al. *Sci. Rep.* **9** 19750 (2019)
507. Melik-Gaykazyan E et al. *ACS Photon.* **5** 728 (2017)
508. Kroychuk M K et al. *Nano Lett.* **20** 3471 (2020)